REPORT DOCUMENTATION PAGE		READ INSTRUCTIONS BEFORE COMPLETING FORM	
1. REPORT NUMBER	2. GOVT ACCESSION NO.	3. RECIPIENT'S CATALOG NUMBER	
4. TITLE *(and Subtitle)* THOMSON BACKSCATTERING FROM AN INTENSE RELATIVISTIC ELECTRON BEAM AS A DIAGNOSTIC FOR A FREE ELECTRON LASER		5. TYPE OF REPORT & PERIOD COVERED Interim	
		6. PERFORMING ORG. REPORT NUMBER 95	
7. AUTHOR(s) S.C. Chen T.C. Marshall		8. CONTRACT OR GRANT NUMBER(s) N00014-79C-0769	
9. PERFORMING ORGANIZATION NAME AND ADDRESS Plasma Physics Laboratory Columbia University New York, NY 10027		10. PROGRAM ELEMENT, PROJECT, TASK AREA & WORK UNIT NUMBERS 61153N RR011-07-0H NR632-002	
11. CONTROLLING OFFICE NAME AND ADDRESS Office of Naval Research 800 N. Quincy Street Arlington, VA 22217		12. REPORT DATE April, 1984	
		13. NUMBER OF PAGES 105	
14. MONITORING AGENCY NAME & ADDRESS*(If different from Controlling Office)* --		15. SECURITY CLASS. *(of this report)* Unclassified	
		15a. DECLASSIFICATION/DOWNGRADING SCHEDULE	

16. DISTRIBUTION STATEMENT *(of this Report)*

Approved for public release; distribution unlimited

17. DISTRIBUTION STATEMENT *(of the abstract entered in Block 20, if different from Report)*

--

18. SUPPLEMENTARY NOTES

--

19. KEY WORDS *(Continue on reverse side if necessary and identify by block number)*

Intense, Relativistic, Electron Beam; Thomson Backscattering, Free Electron Laser

20. ABSTRACT *(Continue on reverse side if necessary and identify by block number)*

Next page

ABSTRACT

THOMSON BACKSCATTERING FROM AN INTENSE RELATIVISTIC ELECTRON BEAM

AS A DIAGNOSTIC FOR A FREE ELECTRON LASER

Shien-Chi Chen

T. C. Marshall

The parallel momentum spread of an intense relativistic electron beam (1 KA/cm^2, 700 KV) used in a Raman free electron laser, is determined by a Thomson backscattering experiment. Theory is reviewed to show that the relativistic effect combines with the backscattering geometry to provide maximum energy resolution, sensitivity, and scattered signal level for the energy diagnostic experiment. The electron beam is field-emitted from a cold cathode, apertured by the anode, and guided by a 9.5 KG magnetic field to scatter the 20 MW peak power, mode-locked 9.6 μm CO_2-laser radiation. The electron beam is found to have adequate qualities for Raman free electron laser applications: A normalized beam energy spread of (0.6 ± 0.14) % is obtained from the frequency-upshifted backscattered spectrum centered at 0.5 μm. It is also found that the use of the 1.7 cm period radially-dependent undulator field introduces extra inhomogeneous broadening on the electron beam -- the momentum spread increases monotonically with the undulator field strength.

Columbia University in the City of New York

THOMSON BACKSCATTERING FROM AN INTENSE RELATIVISTIC ELECTRON BEAM

AS A DIAGNOSTIC FOR A FREE ELECTRON LASER

Shien-Chi Chen   &

T.C. Marshall

1984

THOMSON BACKSCATTERING FROM AN INTENSE RELATIVISTIC ELECTRON BEAM

AS A DIAGNOSTIC FOR A FREE ELECTRON LASER

Shien-Chi Chen   &

T.C. Marshall

1984

Plasma Physics Laboratory
School of Engineering and Applied Sciences
Columbia University
New York, New York 10027

CONTENTS

CONTENTS
(continued)

LIST OF FIGURES

LIST OF FIGURES
(continued)

Chapter I

INTRODUCTION

I-A.   Introductory Remarks

The free electron laser (FEL) has become the subject of intensive research because of its potential as an efficient, high-power source of continuously tunable coherent radiation. The output wavelength is determined by the undulator magnet period and the electron energy (Equation I.2). Section B reviews the principles of the free electron laser.

With the present stage of accelerator and magnet technology, free electron lasers can be designed so that the interaction is dominated either by single particle or collective effects. The crucial parameters that characterize these two operation regimes are the electron beam density and the beam momentum spread in the parallel direction. In order to operate the FEL in the high-gain, high-efficiency collective regime, the electron beam must be cold and dense.

Information about the intense relativistic electron beam (IREB) characteristics in a free electron laser is of major importance in understanding the collective amplification process and the oscillator start-up problems. However experimental data on the beam properties have been rare and the existing diagnostic techniques are inaccurate. Section C serves to place the research of this dissertation in the context of existing work.

A Thomson backscattering experiment (*) was designed to determine the parallel energy spread of the intense relativistic electron beam. A high sensitivity and a high resolving power were achieved in this non-interactive energy spectral system. Measurements were performed with different degrees of undulator excitation, and the results showed that the dense ($\gtrsim 1$ KA/cm^2) electron beam is indeed suitable for the collective free electron laser applications.

(*) S.C. Chen, T.C. Marshall in Phys. Rev. Lett. 52 (1984): 425
S.C. Chen, T.C. Marshall, and S.P. Schlesinger in Proceedings of the Free Electron Laser Workshop (1983), and S. C.Chen, T.C.Marshall, and S.P.Schlesinger in Bulletin of American Physical Society 28 (1983):1062 ; and in Proceedings of LASERS 1982 Conference. See also Davis and Willi in Bulletin of American Physical Society 28 (1983): 1040.

I-B. Free Electron Lasers

The history of the development of the free electron laser
can be traced back to the 1950's, when the generation of narrow-
band radiation was dominated by electron tube technology, and the
unfavorable scaling of these devices with decreasing wavelength
propelled the investigation into other radiation mechanisms. The
spontaneous radiation from a relativistic electron beam moving
through   an   undulator was first   proposed   and   studied
experimentally by the Stanford group (Motz et al., 1951; 1953).
Then in 1959, Motz and Nakamura (1959) showed that the mechanism
can be combined with a waveguide structure to amplify external
waves.   "Ubitrons" were   developed   (Phillips,   1960)   and
demonstrated that high peak power and high efficiency could be
obtained by the undulated beam interaction.   However,   the
"gyrotron" -- the electron cyclotron maser -- has been proved to
be a more efficient microwave source (Schneider, 1959) at $\lambda \lesssim 1$
cm.

With the invention of the laser in the early sixties,
research interests shifted into the new area of quantum
electronics. However, the optical resonator feedback concept in
lasers was introduced into the electron beam devices to replace
the waveguide. The combination of stimulated Compton scattering
process with a feedback structure provides a new lasing mechanism
which was studied by many authors. In 1968, Pantell and coworkers
showed theoretically that a relativistic electron beam "pumped"
by an intense microwave field would amplify the corresponding

Doppler shifted short-wavelength radiation.

Madey (1971) showed in his first "free electron laser" paper that useful gain can be obtained at optical wavelengths and the characteristics of the gain spectrum were studied. The first demonstration of stimulated Compton scattering was carried out at Stanford (Elias et al., 1976), in which 10.6 μm radiation was amplified by the interaction of the SLAC electron beam with a helical undulator field. The first free electron laser operated in the oscillator configuration (see figure I.1) was performed in the next year (Deacon et al., 1977).

Meanwhile, free electron lasers driven by intense relativistic electron beams were also studied intensively. The first series of experiments using static magnetic undulator for exitation of the Raman scattering process was conducted at Columbia University (Efthimion and Schlesinger, 1976). The linear dependence of growth rate on the pump amplitude was demonstrated by Marshall (1977), in which several MW of mm radiation was generated. Detailed spectroscopic studies of the radiation were carried out by Gilgenbach (1979). McDermott (1978) reported on the realization of a collective Raman FEL oscillator. (The different operating regimes of a free electron laser are outlined in the following sections.)

Research activity in FEL increased greatly in the early 1980's: multicomponent FEL for efficiency enhancement in amplifiers ; amplification of visible light in a storage ring FEL; construction of FIR FELs at Bell Laboratories and Frascati; an electron beam recycling experiment and the preparation for a two-stage FEL were in progress at UC Santa Barbara; and the
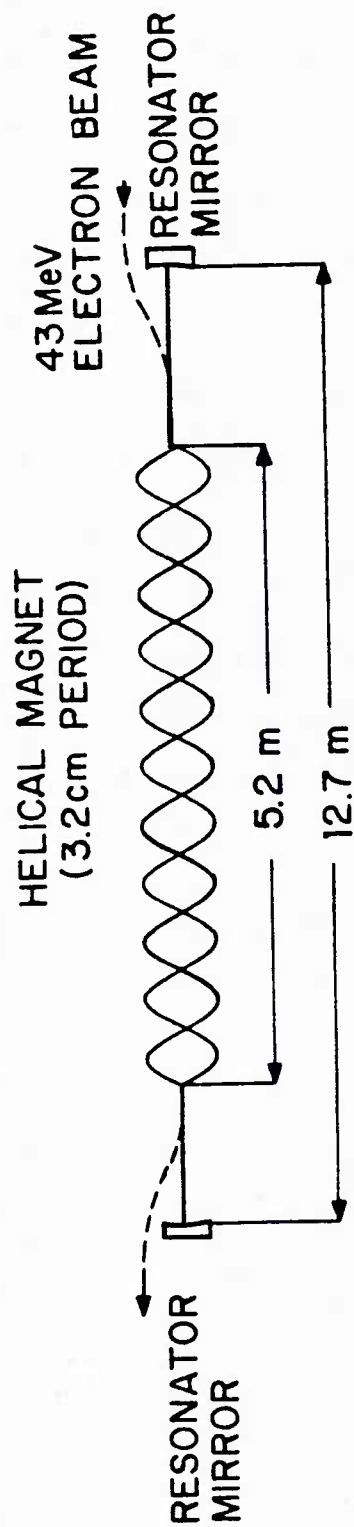
Figure I.1   Schematic of the first free electron laser
(After Deacon, et al., 1977)

construction of storage ring FEL facilities (ACO in France, ADONE in Italy, and at Brookhaven and Stanford in the USA).

Conventional lasers are very powerful research tools in general, but because of the lack of physical lasing mechanisms and the lack of proper optical components, there are still some spectral bands in the coherent radiation spectrum that are not covered by conventional lasers, namely in the FIR, XUV, and shorter wavelength regions. The free electron laser has the potential to fill these gaps through the use of different accelerator-undulator combinations. Frequency tunability over apprximately one decade is expected for each particular combination. The free electron laser can also provide pico-second pulses since the output structure depends directly on the electron pulse structure (in high energy accelerators, the electrons usually are generated in short micro-pulses); this is an important feature for transient and non-linear studies.

I-B-1   Single particle FEL

The free electron laser is a linear fast-wave device in which a signal wave is amplified at the expense of the axial kinetic energy of a relativistic electron beam through the interaction with a preprogramed, periodic, external "undulator" field (see Fig. I.1). The basic gain mechanism of a free electron laser (FEL) is easily understood by a single-particle description, in which a relativistic electron ($\beta = v/c$) travels through a static, spatially periodic transverse magnetic field $\vec{B}_\perp$

(the undulator). The electrons are "wiggled" by the field with a transverse velocity $\vec{v}_\perp$ and oscillate in trajectories with the same longitudinal periodicity as the undulator (ℓ). The undulating electron beam can be used to amplify electromagnetic radiation of certain frequency (w_s) propagated in the same direction as the electron beam. The EM signal can be the spontaneous radiation emitted by other electrons, or any external radiation sent in to be amplified.

The EM field ($\vec{E_s}$, $\vec{B_s}$) exchanges energy with the electrons at the rate $\vec{v}_\perp \cdot \vec{E_s}$ (See for example, Colson, 1977). The energy exchange interaction is near optimum when $\vec{v}_\perp$ and $\vec{E_s}$ are synchronized in such a way that exactly one wavelength of signal radiation passes over the electron as the electron traverses one period of magnet, so that $\vec{v}_\perp$ and $\vec{E_s}$ remain in phase throughout the interaction length L. This resonance condition relates the basic parameters of the system :

$$\beta = \beta_0 = \frac{\omega_s}{\omega_s + 2\pi c / \ell} \qquad (I.1)$$

and determines the wavelength that is amplified (or absorbed):

$$\lambda_s = \frac{\ell}{2\,\gamma_\parallel^2} \qquad (I.2)$$

, where $\gamma_\parallel^2 = 1 \, / \, (1 - v_\parallel^2/c^2)$.

The initial phase between the electron and the radiation field determines whether the process is stimulated emission or stimulated absorption. Suppose the electrons are distributed

uniformly along the axial direction: the contributions to the gain from these randomly phased electrons cancel out and result in zero energy exchange. To obtain net gain , it is necessary to bunch the electron beam properly in the longitudinal direction. The ponderomotive potential well ($\vec{v}_\perp \times \vec{B}_S$) provides such a mechanism to trap electrons and modulate the electron density by forming bunches.

Gain results from bunching when electrons are injected into the interaction region with a velocity slightly higher than the resonant velocity given by equation I.2, so that after traversing the undulator length L, the electron beam loses net energy to the signal field.

The gain bandwidth of the free electron laser is broadened homogeneously by the non-monochromatic pump wave (finite number of undulator periods leads to an indeterminacy of the pump frequency $\Delta w/w \sim 1/N$), and inhomogeneously by the parallel momentum spread of the electrons. In operation, the laser linewidth is further narrowed by the use of an optical resonator.

The polarization of the free electron laser output is determined by the polarization of the undulator magnet. In general, a helical magnet amplifies circularly polarized light, while a planar (linearly polarized) magnet amplifies linearly polarized waves.

In the classical picture, the principle of operation of an FEL can be summarized as follows: the undulator magnet and the radiation field combine to modulate the relativistic electron beam at the signal wavelength, and the electron kinetic energy is extracted coherently in the form of radiation with the same

wavelength.

It is also interesting to describe the wave-particle interaction using quantum electrodynamic language. In the electron rest frame, the undulator magnetic field appears as an EM wave with a frequency $\omega_i' \cong 2\pi\gamma c/\ell$, while the signal wave is Doppler downshifted in frequency $\omega_s' = \omega_s/2\gamma$, where the primed quantities are measured in the rest frame of the electron. These two waves impinge on the electron from opposite direction.

Without the signal wave, the undulator wave is Compton scattered by the electron and produces spontaneous emission. The stimulated Compton process takes place when a signal wave of the right frequency is also involved. If $\omega_s' = \omega_i'$ then the electron does not recoil after the two-wave interaction, and no net gain is achieved since the scattering cross section is the same for stimulated emission and absorption. If we arrange the parameters so that there is a small frequency difference between w_s' and w_i' (to be taken up by the electron recoil), then depending on the sign of the frequency difference , either stimulated emission (electron decelerated) or stimulated absorption (electron accelerated) is energetically favored. In other words, the gain of these two processes peak at different frequencies (although they share the same matrix element), and the resultant gain spectrum (anti-symmetric about w_i') is the difference of these two line shape functions. A quantitative derivation leads to the famous free electron laser theorem - the gain spectrum of a two-wave FEL is proportional to the first derivative of the spontaneous spectrum (Madey, 1971 and Madey, 1979).

The quantum calculation in the original FEL theory paper (Madey,1971) showed the gain formula does not depend on $\hbar$, and motivated the subsequent efforts in developing a pure classical theory (*). Until now, classical theory is proved to be more useful in describing non-linear effects (such as pulse slippage) and plasma effects. Quantized fields and quantized electrons (as wave packets) are necessary only for limiting cases. It should be noted that even in the absense of electron recoil, (viz, $\hbar \rightarrow 0$), gain is still obtained for systems of finite undulator length.

There are several names for free electron lasers operated on the principle described in this section : the "single particle FEL", or the "Compton regime FEL", and the "two-wave (one particle) FEL" . The first operation of a single particle FEL was demonstrated by the Stanford University group (Deacon et al., 1977).

(*) See for example W.B. Colson, 1977, 1980; F.A. Hopf, P. Meyste, G.T. Moore, and M.O. Scully, 1977 ; N.M. Kroll, 1977; H.P. Freund and P. Sprangle, 1981; W.B.Colson, 1982.

I-B-2   Collective FEL

With the recent development of accelerators capable of generating high current and high voltage electron beams, (e.g. induction linear accelerator , pulsed transmission line) research has been moving toward free electron lasers driven by intense relativistic electron beams (IREBs). Although the basic components used in the intense-beam free electron lasers are similar to that of the single particle FELs, the gain mechanisms involved are quite different.

As the electron density in the beam increases beyond certain limit (either by bunching or by using high current beams) , neighbouring electrons interact strongly through the Coulomb force to the extent that the electrons lose their individual particle identities and begin to respond to the external EM excitations as a collective entity. In the interaction of the undulator magnet and the radiation field, it is possible to excite a wave in the "electron plasma" under appropriate conditions. To be more precise, if in the beam frame the frequency difference between the undulator wave and the signal wave is chosen to match one of the plasma normal mode frequencies, then the excitation of a third wave is possible. In the collective case the emission of the "plasmon" substitutes for the Compton recoil in the single particle case. This resonant interaction permits the signal to grow exponentially along an undulator of arbitrary length.

The collective FEL interaction involves three waves: the

pump wave (undulator), the scattered wave, and the idler wave (usually the electron beam space charge wave). The pump wave can decay into one scattered wave and one space charge wave, hence this three-wave interaction completely parallels the stimulated Raman scattering process; accordingly, the collective FEL is also called the "Raman FEL" or "Three-wave FEL".

The collective FEL has an exponential growth along the beam direction, and there is no limit to the length of the system as long as the beam remains synchronized with the waves, so higher gain and efficiency (a few %) are expected . In contrast, the Compton regime FEL with uniform undulator is characterized by finite length, low gain and low energy extraction efficiency (< 1 %), which is limited by the nature of the single particle interactions.

However, operation of an FEL in the Raman regime requires additional consideration. First, the wave excited in the electrons must qualify as a wave, that is, the wavelength has to be short enough so that there are many oscillations present along the system length at any instant

$$\omega_p \cdot \left(\frac{L}{\gamma c} \right) \gg 1 \qquad\qquad (I.3)$$

where ω_p is the plasma frequency in the beam frame. This relation sets a lower limit on the beam density. Second, to maintain a parametric decay process like this , at least the three constituents have to remain intact even without interaction. The non-depleting pump wave and the EM signal wave satisfy this requirement automatically. But the mediating space charge wave is easily Landau-damped if the electron velocity

distribution is too broad. The damping of the idler wave weakens the coupling between the three waves and reduces the growth rate. The finite-temperature effect in Raman free electron lasers was studied theoretically (Ibanez and Johnston, 1983), and it was found that the electron beam parallel momentum spread is a very critical factor. Furthermore, the efficiency of the Raman FEL deteriorates dramatically as the energy spread increases (Kwan and Snell, 1983).

The cold beam requirement can also be argued as follows: to expect any collective behavior from the electrons, the Debye length of the electron plasma must be much shorter than the ponderomotive (plasma) wavelength involved so that many electrons interact with the same period of the signal wave simultaneously. This requirement sets an upper limit on the tolerable electron beam energy spread in the parallel direction

$$\left(\delta\gamma/\gamma \right)_{\parallel} \lesssim \left(\frac{\ell}{2\gamma}\right) \cdot \left(\frac{\omega_p}{2c}\right) \sim \frac{1}{N} \quad ; \qquad (I.4)$$

for the Columbia FEL parameters, this limit is about 2 %.

I-C   Thomson Backscattering Experiment

In order to operate the Raman free electron laser with high gain and high efficiency, the electron beam must be "dense" and "cold" (See equation (I.3) and (I.4)). For our case, the beam (1 KA/cm^2) is dense enough, while the energy spread from all

sources (Section I-D) should be held to a value below 2 %.

However, such a high quality beam is not easily available since the accelerator technology for intense relativistic electron beam (IREB) is not as well developed as that of the synchrotrons and the RF linear accelerators which are typically used to drive Compton FELs. The high current electron beam is usually generated by a field-emission vacuum diode (See III-C) . A finite (and relatively large) velocity spread is usually associated with the beam and is not easily minimized as in the case of thermionic electron guns. On the other hand, considerable effort has been devoted to develope a high quality beam in this configuration, either through the use of high magnetic fields (McDermott, 1978; Sheffield et al., 1982) or by aperturing (Jackson, 1983). We want to know if the beam thereby generated has adequate quality for a Raman FEL.

Moreover, experimental data on the intense relativistic electron beam is extremely hard to obtain. The magnet spectrometer typically used to diagnose the high energy low current electron beam is not suitable for this purpose. The imaging technique with a "pepper pot" mask is good only for observing the small beam emittance and the rotation of a tenuous beam. Although there have been experiments designed to measure the intense beam quality using direct or indirect methods, they all rely on interactive techniques: in one measurement (Avivi, Cohen, and Friedland, 1983), a section of quartz tube is inserted into the drift tube to measure the radial electrostatic potential induced by the space charge of the beam. The averaged axial velocity is proportional to the ratio of the beam current to the

voltage across the quartz capacitor. This technique alone cannot yield information about the velocity spread. Another experiment (Shefer, Yin, and Bekefi, 1983) combines the above $\langle v_{\shortparallel} \rangle$ measurement with a second dianostic: measurement of the beam cyclotron wavelength in the guiding magnetic field, which yields a spatially averaged product $\langle \gamma v_{\shortparallel} \rangle$, where $\gamma^2 = (1 - v_{\shortparallel}^2/c^2 - v_{\perp}^2/c^2)^{-1}$. A small pinhole aperture is placed in the path of the beam, and a moveable current collector is located downstream of the pinhole. The observed periodicity of the collected current allows one to calculate the product $\langle \gamma v_{\shortparallel} \rangle$ in the beam. In principle, the velocity spread can be inferred indirectly from the width of the current peaks in the periodic spatial dependence curve. However, this method is not sensitive to a small energy spread and does not provide the resolving power necessary for diagnosing high quality beams (the graphite needle cathode in their experiment produces a "hot" <large emittance> beam).

A diagnostic reported by Friedman (1973), using a diamagnetic loop and magnetic probes, measured a transverse energy of 15 KeV for a 600 KeV electron beam.

A deflecting magnet momentum analyzer ($\Delta E/E \lesssim 1$ %) was utilized to study the discrete energy spectrum of an apertured IREB (Kawai, Kawamura, and Toyoda, 1983), in which a 1 mm sampling slit is placed in the beam path. The observed energy spectrum showed a narrow multiple-"line" structure, with a total beam energy spread of $\sim$ 10 %. This is typical of diodes assembled without any special design considerations.

An apertured diode was carefully designed (Jackson et al.,

1983., also see section III-C) to generate a low emittance beam, and the momentum spread was obtained experimentally. For this purpose, the anode aperture was extended by 15 cm into a uniform diameter drift tube which terminated in a Faraday cup, so that only those electrons for which the sum of the Larmor and guiding center radii is less than the aperture radius could be propagated. The transmitted current as a function of the guiding field intensity yields information on the electron transverse velocity distribution. The axial velocity spread is obtained by assuming the electrons to be monoenergetic. However, the effect of the undulator excitation cannot be studied simultaneously by this simple arrangement.

These measurements all rely on interactive methods (slits, pinholes, dielectric capacitors, extended anodes) and do not provide the sensitivity and accuracy needed to diagnose a high quality beam in Raman FEL .

What is needed is a non-interactive technique capable of determining the energy spread of the entire beam in real FEL environment with an energy resolution of about 0.1 %. Such an energy diagnostic spectral system is essential for obtaining knowledge on how well an intense relativistic electron beam will meet the "Raman FEL cold beam criterion" (Equation I.4). This also provides a quantitative basis for interpreting a Raman FEL amplifier experiment.

A Thomson backscattering experiment, which forms the principal part for this thesis, was set up, in which the infrared radiation (20 MW at 9.6 μm) is sent into the FEL against the electron beam flow (700 KV, 1 KA/cm^2), and observation is made in

the backscattered direction. The observed spectrum (centered at 0.5 μm) is upshifted by a factor of about 20 and carries the information of the electron parallel velocity distribution.

The Thomson backscattering technique is a very good tool for diagnosing the intense relativistic electron beam for two reasons: (1) it takes advantage of the relativistic effects and the backscattering geometry in a consistent way (See chapter II) to obtain maximum signal level, resolving power, and sensitivity; (2) it benifits from the high electron density of the beam, without which the experiment is impossible.

The experiment was also performed to measure the effect of the radially-nonuniform undulator field on the beam energy spread. In the next section the various major mechanisms responsible for beam energy spread (and contribute to the observed spectrum broadening) are described.

I-D   Mechanisms of Inhomogeneous Broadening

There are many possible mechanisms that act on each electron individually, and result in a beam momentum (or energy) spread in the parallel direction. Listed in this section are those which seem to be common for most free electron lasers.

(a) Effects Of The Undulator

The magnectic field in a double-helical winding undulator

is calculated by Blewett and Chasman (1977) for $2\pi r/\ell < 0.8$

$$B_r \cong B_\perp \cdot \left(1 + \frac{3}{8}\left(\frac{2\pi r}{\ell}\right)^2 + \cdots\right) \cdot \sin\left(\frac{2\pi z}{\ell} + \theta_0\right) \tag{I.5}$$

$$B_\theta \cong B_\perp \cdot \left(1 + \frac{1}{8}\left(\frac{2\pi r}{\ell}\right)^2 + \cdots\right) \cdot \cos\left(\frac{2\pi z}{\ell} + \theta_0\right) \tag{I.6}$$

$$B_z \cong B_\perp \cdot \left(-\frac{2\pi r}{\ell}\right) \cdot \left(1 + \frac{1}{8}\left(\frac{2\pi r}{\ell}\right)^2 + \cdots\right) \cos\left(\frac{2\pi z}{\ell} + \theta_0\right) \tag{I.7}$$

The radial inhomogenity of the field causes the electrons in different orbits to be pumped to different degrees

$$\beta_\perp(r) = \frac{e\, B_\perp(r)\, \ell}{2\pi m c^2} \cdot \frac{1}{\gamma} \equiv \frac{a_w(r)}{\gamma} \tag{I.8}$$

The parallel energy spread induced by the pump field with radial gradient $\Delta B_\perp/B_\perp$ over the beam, is:

$$\left(\frac{\delta\gamma}{\gamma}\right)_{\parallel,\,und} \cong \left(\frac{e\, B_\perp\, \ell}{2\pi m c^2}\right)^2 \cdot \left|\frac{e B_0 \ell}{m c^2 \gamma\, 2\pi} - 1\right|^{-2} \cdot \left(\frac{\Delta B_\perp}{B_\perp}\right) \tag{I.9}.$$

The term in the absolute value brackets is the enhancement factor for a system operating near the magnetoresonance of the guiding field $\vec{B}_0$.

(b) Beam Emittance

In principle, electrons are accelerated to the same accelerator energy when they enter the interaction region. However, during the beam generation and acceleration processes, a finite spread in the transverse velocity

components is always associated with the diode geometry and the configuration of the accelerating electrodes. If the spread of trajectories involves an average divergence angle $\sqrt{\langle \theta^2 \rangle}$, the normalized emittance (see Neil, 1979) of the beam is defined as

$$\varepsilon_N \equiv \gamma \beta \pi r_b \sqrt{\langle \theta^2 \rangle} \qquad (I.10)$$

where r_b is the radius of the beam. The emittance parameterizes the distribution of transverse motion in the beam, which is itself related to the parallel energy spread :

$$\left(\frac{\delta \gamma}{\gamma}\right)_{\parallel, \varepsilon} \cong \frac{1}{2}\left(\frac{\varepsilon_N}{r_b}\right)^2 \frac{1}{1 + a_w^2} \qquad (I.11)$$

(c) Electron Beam Space Charge

The Coulomb repulsion between the charges in the beam results in a "laminar" change of electron parallel energy across the beam. For a solid beam the spread is

$$\left(\frac{\delta \gamma}{\gamma}\right)_{\parallel, s.c.} \simeq \frac{\omega_{po}^2 \, r_b^2}{4 \gamma c^2} \qquad (I.12)$$

where r_b is the radius of the beam, and $\omega_{po}^2 = 4\pi n e^2 / m_o$.

On the other hand, beam rotation ($\vec{E_r} \times \vec{B_z}$) causes a decrease of electron parallel motion on the outside of the beam -- as the rotation velocity is proportional to the beam radius for rigid rotor motion. This effect tends to

compensate for the space charge depression effect:

$$\left(\delta\gamma/\gamma\right)_{\parallel,s.c.} \cong \frac{\omega_{po}^2 r_b^2}{4\gamma c^2}\left(1 - \frac{2\omega_{po}^2}{\Omega_o^2\gamma}\right) \qquad (I.13)$$

where $\Omega_o = \frac{eB_o}{mc}$. However, this rigid rotor equilibrium is not easy to set up in real experiment, nor is it possible to choose ω_{po} large enough to reduce $\left(\delta\gamma/\gamma\right)_{\parallel,s.c.}$ to zero.

These three inhomogeneous broadening processes combine to form the total scattered spectral width. If these mechanisms operate on the electrons in an independent fashion, then

$$\left(\Delta\omega/\omega\right)_{inhomo} = \sqrt{\left(\Delta\omega/\omega\right)_{\epsilon}^2 + \left(\Delta\omega/\omega\right)_{s.c.} + \left(\Delta\omega/\omega\right)_{und}^2} \qquad (I.14)$$

This dissertation reviews the relativistic Thomson scattering theory and records the design considerations , difficulties , and results of the scattering experiment.

The scattering cross sections are derived in chapter II from both classical and quantum mechanical approaches with emphases on the features unique to the backscattering geometry.

The major components of the experiment are described in chapter III. Chapter IV describes the complicating difficulties together with the corresponding techniques used to solve them.

Chapter V presents the results of the experimental investigations, followed by a short discussion and conclusion in chapter VI.

Chapter II

THEORY OF RELATIVISTIC THOMSON SCATTERING

II-A   Introduction

The differential scattering cross section for relativistic Thomson scattering is derived both classically and quantum mechanically in section B, and are shown to be mutually consistent. The angular distribution of the scattering intensity and the scattered spectrum are described in detail, and the unique features for the backscattering geometry are revealed : The differential cross section is enhanced by a factor of $4\gamma^2$, with a maximized frequency upshift of $4\gamma^2$. The sensitivity for resolving small parallel energy spread is also a maximum at this observation angle. In addition, the backscattering technique offers the best resolution for observing the spectrum over a finite solid angle.

The scattered radiation carries the information of the electron velocity distribution. The relation between   the scattered spectral width and the electron beam energy spread for the incoherent scattering is described in section C.

Section D briefly reviews the photon polarization effect and the electron finite-residence-time effect. The correct treatment of both effects is essential for obtaining a single particle scattering cross section suitable for direct averaging over the electron velocity distribution. An erroneous treatment of the finite-volum effect has been propagated in   the literature. The confusion was not cleared up until very recently.

II-B   Calculation of Cross Sections

III-B-1   Quantum Electrodynamic derivation

This section contains the quantum electrodynamic (QED) derivation of the relativistic Thomson scattering cross section, which is the Compton scattering in the limit of low photon energy.

The lowest order contribution comes from the second order terms (Figure II.1), with one vertex responsible for absorption, and the other vertex for emission. The differential cross section (*) for Compton process (see Bjorken and Drell) was calculated to be

$$\frac{d\sigma}{d\Omega} = \frac{r_o^2}{2\gamma^2} \frac{X}{(1 - \vec{\beta}\cdot\hat{k}_c)^2} \left(\frac{\omega_s}{\omega_i}\right)^2 \qquad (II.1)$$

where $r_o = e^2/4\pi m = 2.8 \times 10^{-13}$ cm = classical electron radius, $\vec{\beta}$ is the velocity vector of the electron normalized to the speed of light. $\vec{K}_i$ and $\vec{K}_s$ are the wave vectors of the incident and scattered radiation. w_i and w_s are the angular frequencies of the incident and scattered radiation, respectively. The initial and final spin states are not observed in the scattering experiment,

----

(*) The cross section in QED gives the event rate, and is a measure of the number of photons scattered into the unit solid angle; whereas the classical cross section gives the power, and is a measure of scattered energy.
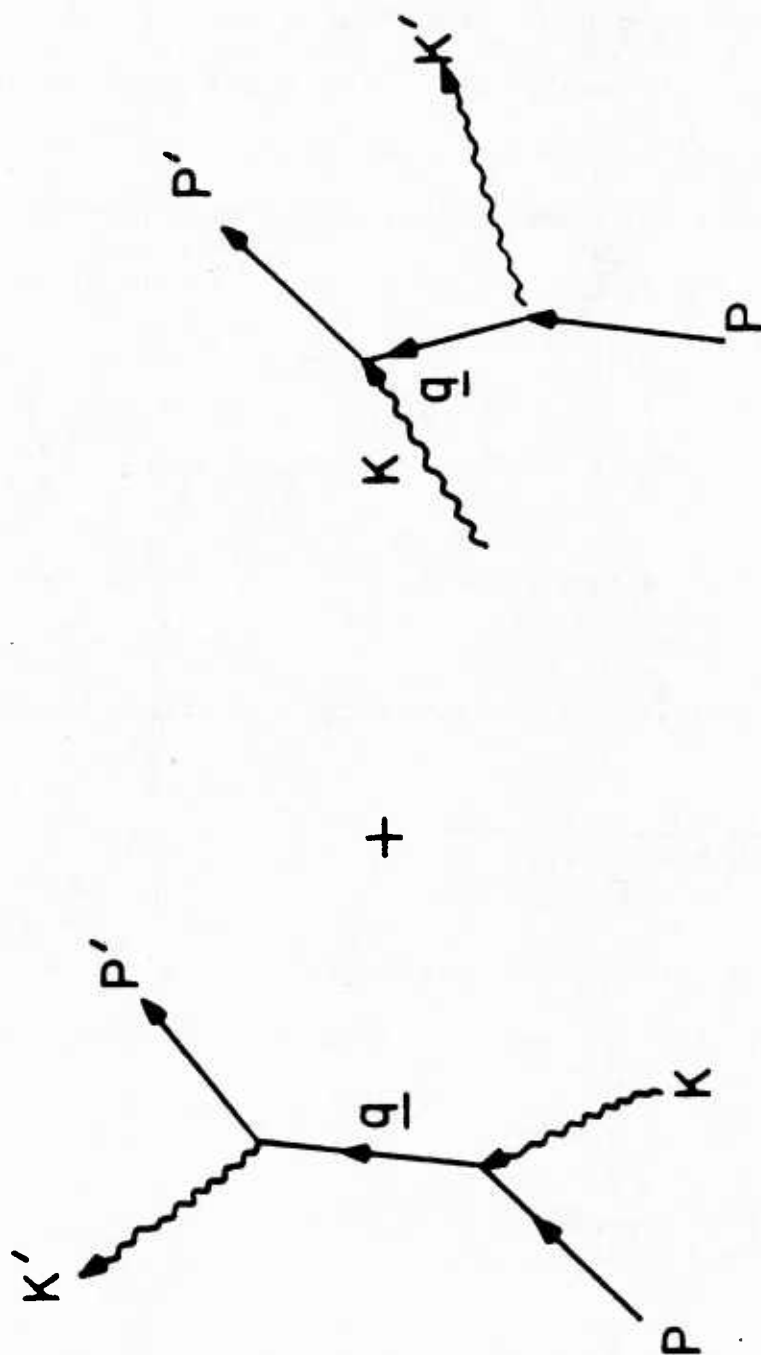
Figure II.1 Lowest order diagrams for Compton scattering

so the sum over final spin states are carried out , results in

$$X = \tfrac{1}{2}(\tfrac{K'}{K}+\tfrac{K}{K'}) - 1 + 2(e \cdot e')^2 + \left[\frac{(e \cdot p)^2 (e' \cdot p')^2}{K^2} + \frac{(e' \cdot p)^2 (e \cdot p')^2}{K'^2} \right]$$

$$+ 4 \left[\left(\frac{e \cdot p \; e' \cdot p'}{K} - \frac{e \cdot p' \; e' \cdot p}{K'} \right) e \cdot e' - \frac{e \cdot p \; e \cdot p' \; e' \cdot p \; e' \cdot p'}{K K'} \right] \qquad (II.2)$$

In the expression p and p are the momentum four vectors of the incoming and outgoing electrons; e and e' are the polarization four vectors of the incoming and scattered photons; κ and κ' are the scalar products between the electron and photon momentum four vectors of the incoming and outgoing pairs. $(\epsilon \equiv \gamma m c^2)$

$$K = -p \cdot k = -p' \cdot k' = \epsilon \, \omega_i (1 - \vec{\beta} \cdot \hat{k}_i) \qquad (II.3)$$

$$K' = -p' \cdot k = -p \cdot k' = \epsilon \, \omega_s (1 - \vec{\beta} \cdot \hat{k}_s) \qquad (II.4)$$

From momentum conservation, the frequency upshift is found to be

$$\frac{\omega_s}{\omega_i} = \frac{(1 - \vec{\beta} \cdot \hat{k}_i)}{(1 - \vec{\beta} \cdot \hat{k}_s) + (\frac{\omega_i}{\epsilon})(1 - \hat{k}_i \cdot \hat{k}_s)} \qquad (II.5)$$

In practical cases the polarizations of the photons are not observed, equation (II.1) must be summed over the final and averaged over the initial polarizations, and the result becomes

$$\left(\frac{d\sigma}{d\Omega}\right) = \frac{\gamma_0^2}{2\gamma^2 (1 - \vec{\beta} \cdot \hat{k}_i)^2} \left(\frac{\omega_s}{\omega_i}\right)^2 \left[\frac{K}{K'} + \frac{K'}{K} + 2\left(\frac{m^2}{K} - \frac{m^2}{K'}\right) + \left(\frac{m^2}{K} - \frac{m^2}{K'}\right)^2 \right] \qquad (II.6)$$

This expression can be rewritten in terms of the ordinary vectors shown in figure II.2, and with the terms of $O\left(\left(\frac{\omega_i}{\epsilon}\right)^2 \right)$ neglected:
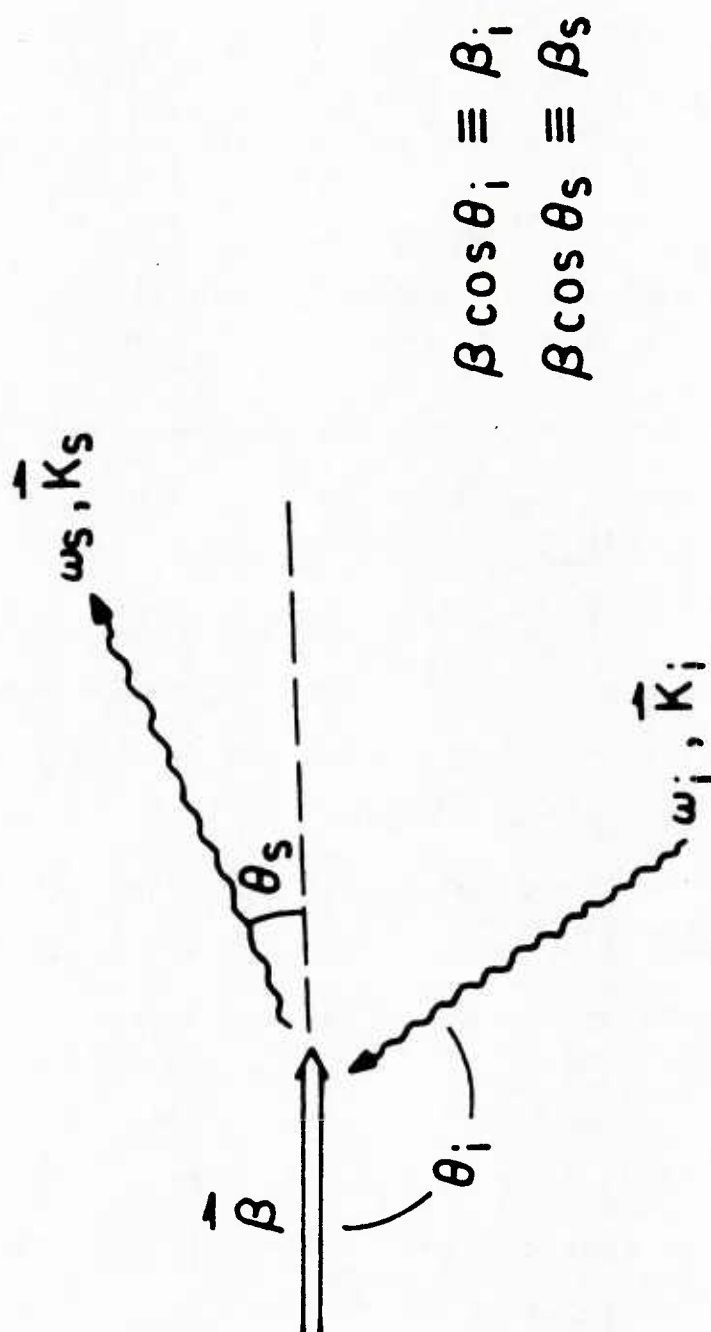
Figure II.2 Thomson scattering shown in ordinary coordinates

$$\frac{d\sigma}{d\Omega} = \frac{r_0{}^2}{2\gamma^2(1-\vec{\beta}\cdot\hat{k}_s)^2} \left\{ \left[1 - \frac{1-\hat{k}_i\cdot\hat{k}_s}{\gamma^2(1-\vec{\beta}\cdot\hat{k}_i)(1-\vec{\beta}\cdot\hat{k}_s)} \right]^2 + 1 \right\} \quad (II.7)$$

The angular dependence of the frequncy upshift (II.5) and the differential cross section (II.7) are highly anisotropic for scattering at relativistic energies, and provide some desirable features for experiments of this nature.

III-B-2   Angular Dependence of Frequency Upshift

For low incidence photon energy $\omega_i/\epsilon \ll 1$, equation II.5 becomes

$$\frac{\omega_s}{\omega_i} = \frac{1 - \beta \cos\theta_i}{1 - \beta \cos\theta_s} \quad (II.8)$$

for a particular choice of incidence angle, the frequency shift as a function of scattered angle (θ_s), is an ellipse with β as eccentricity, and with a major axis of $(1-\beta_i)2\gamma^2$. Polar spectra for β = 0.89, 0.90, 0.91 are shown in figure II.3 for $\theta_i = \pi$. The case of zero electron velocity, the dipole radiation case, appears as a unit circle around the origion.

Some interesting facts are noted here:

(1) The most pronounced frequency upshift is observed in the θ_s = 0 direction. An upshift factor of 4 γ^2 is obtained for the geometry used in the experiment.

(2) Since $\left. \frac{\partial \left(\frac{\Delta\omega}{\omega}\right)_{inhomo}}{\partial \theta_s} \right|_{\theta_s=0} = 0$, the scattered spectrum is stable for first
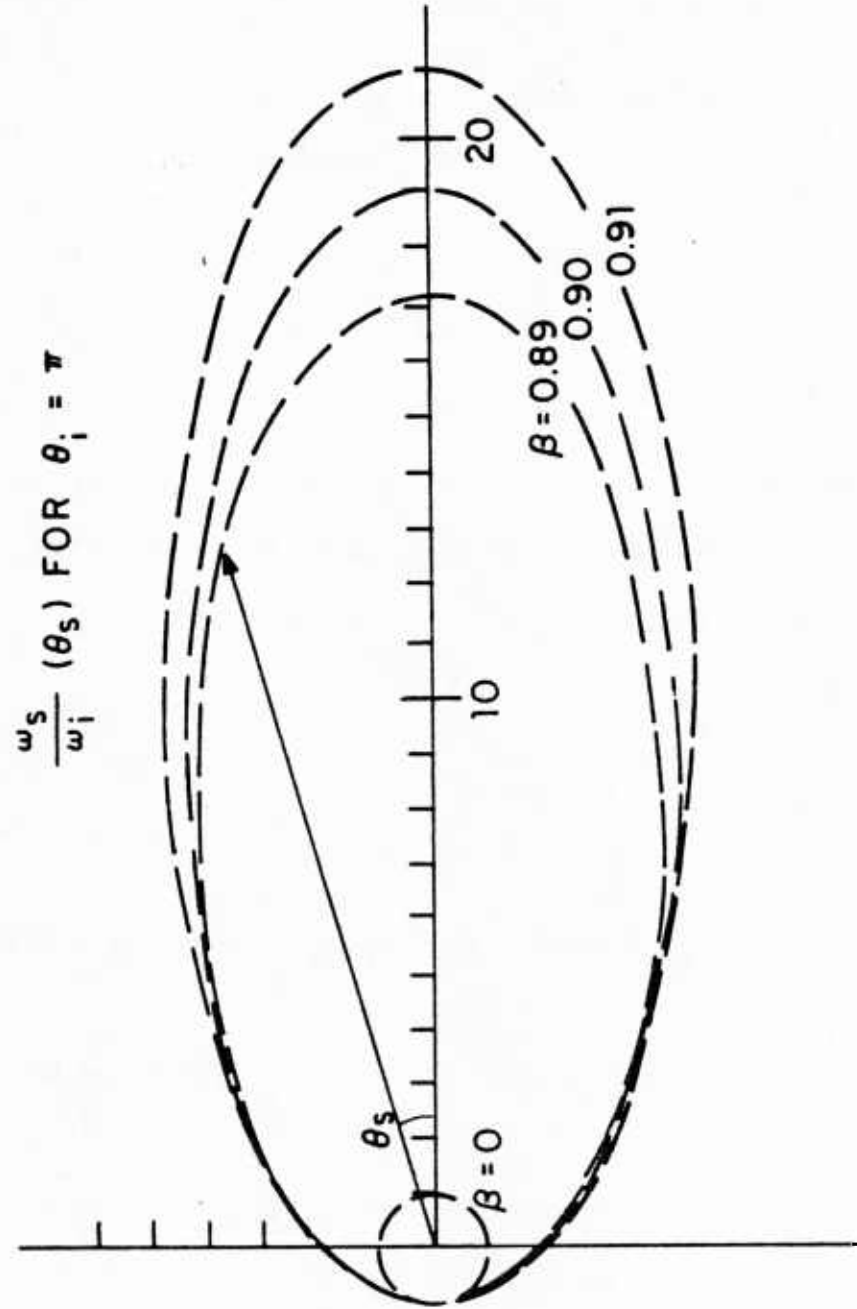
Figure II.3 Dependence of frequency upshift on scattered angle for various electron velocities

order variation over θ_s, which means the half angle of the observation cone $d\Omega$ can be extended reasonably for a larger signal level without introducing a significant amount of angular broadening which limits the resolving power

$$\left(\frac{\Delta\omega}{\omega}\right)_{\Omega} \cong -\gamma^2 (\Delta\theta_s)^2 \qquad (II.9)$$

For an optical system with an f# of about 30, a spectral resolution of $\left(\frac{\Delta\omega}{\omega}\right)_{\Omega} \sim 0.1$ % is achievable in the $\theta_s = 0$ direction.

(3) The inhomogeneous broadening owing to various electron velocity components is resolved most effectively in $\theta_s = 0$ direction. This fact is demonstrated in the following equation

$$\left(\frac{\Delta\omega}{\omega}\right)_{inhomo} = \left(\frac{\Delta\beta}{\beta}\right)\left(\frac{\beta\cos\theta_s}{1-\beta\cos\theta_s} - \frac{\beta\cos\theta_i}{1-\beta\cos\theta_i}\right) \qquad (II.10)$$

which maximizes at $\theta_s = 0$ for a particular velocity spread.

These three features make $\theta_s = 0$ a desirable observation direction.

The dependence of frequency upshift on incidence angle is plotted in figure II-4 for the $\theta_s = 0$ case . They belong to a family of cardioids. The curves with $\beta = 0.9$ and 0.8 are shown. Maximum upshift occurs when $\theta_i = 180°$ (head-on scattering). The inhomogeneous broadening $\left(\frac{\Delta\omega}{\omega}\right)_{inhomo}$ is resolved most effectively at this incidence angle.
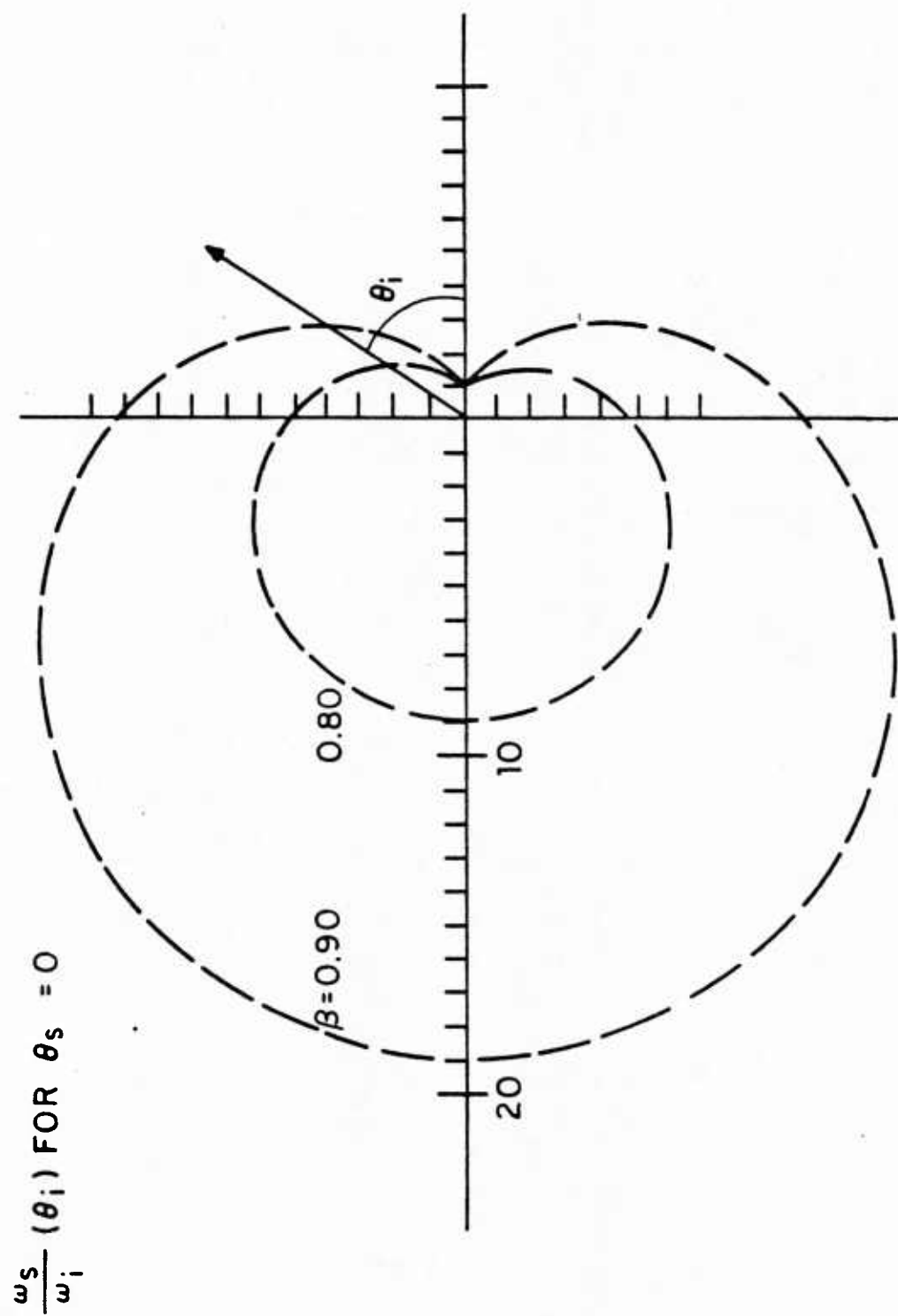
Figure II.4   Dependence of frequency upshift on incident angle
for various electron velocities ..

III-B-3   Angular Dependence of Cross Section

Equation II.7 describes the scattering probability of a "one photon-one electron" system. To estimate the scattered photon number for experiments with streaming electrons interacting with the incident photon flux, this cross section has to be multiplied by the electron density, incident photon density, and by a geometrical factor that describes the relative orientation of these two beams (see Akhiezer and Beresteskii). After multiplying by the "flux compression factor" $(1-\vec{\beta}\cdot\hat{k}_i)$, equation II.7 becomes

$$\frac{d\sigma}{d\Omega} = \frac{r_0^2(1-\beta_i)}{2\gamma^2(1-\beta_s)^2} \left\{ \left[1 - \frac{1-\hat{k}_i\cdot\hat{k}_s}{\gamma^2(1-\beta_i)(1-\beta_s)} \right]^2 + 1 \right\} \qquad (II.11)$$

For the case of practical interest in laser plasma diagnostics, viz, with the incidence and observation beam lines orthogonal to each other, and for the special case of our backscattering experiment, the term in the large parenthesis can be approximated by 2

$$\frac{d\sigma}{d\Omega} \cong \frac{r_0^2}{\gamma^2} \frac{(1-\beta_i)}{(1-\beta_s)^2} \qquad (II.12)$$

Equation II.11 and II.12 are plotted as a function of scattered angle (in polar coordinates) in figure II.5 for the case of $\beta = 0.9$ and $\theta_i = \pi$. The dotted curve is the trace of equation II.12, which is a good approximation of eq II.11 for small observation angles.
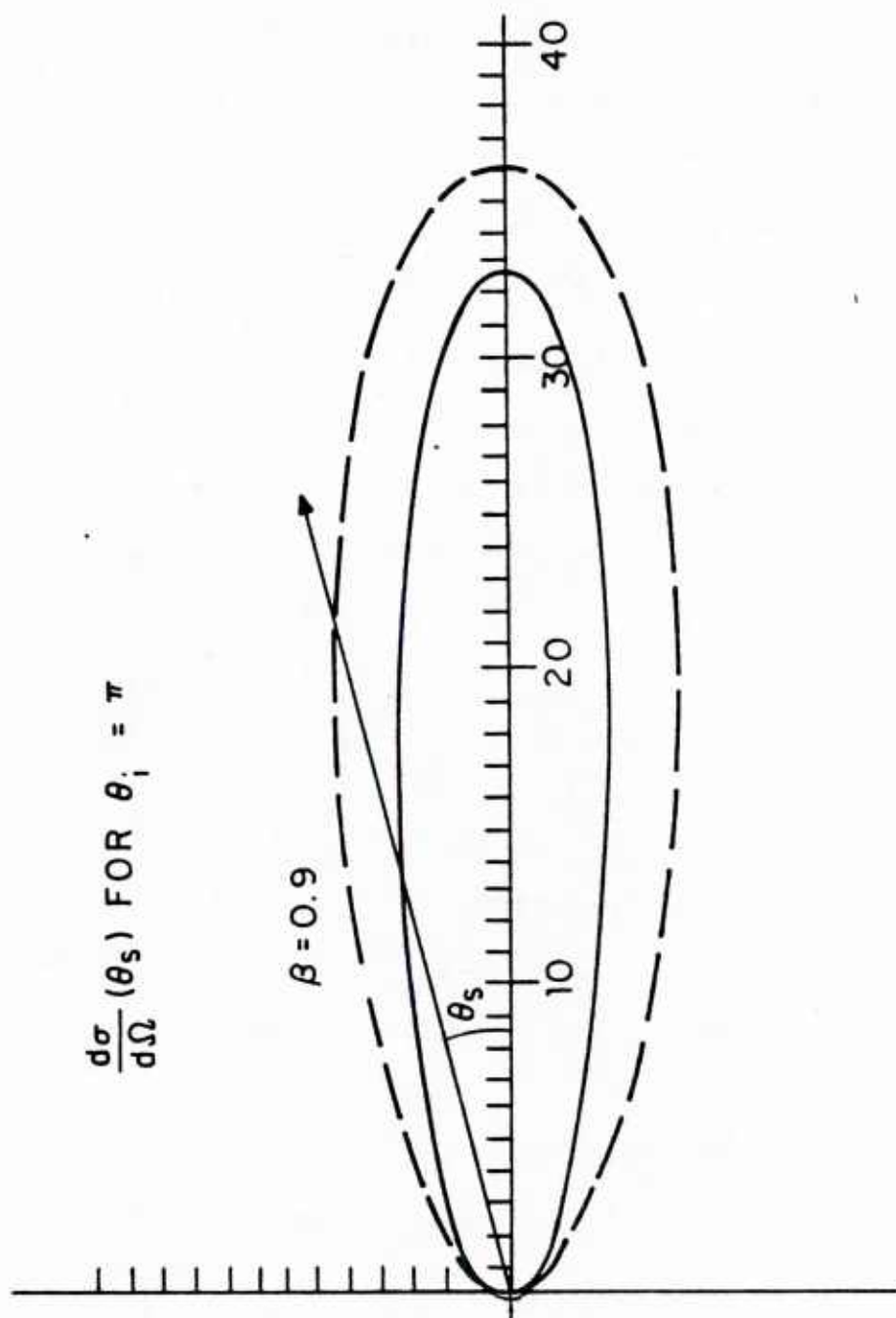
Figure II.5 Dependence of scattering cross section on scattered
angle for exact and approximated expressions .

This angular dependence shows a dramatic enhancement of interaction in the electron beam direction. This cross section enhancement, together with the three features mentioned in last section -- maximized frequency upshift; spectral sensitivity; and maximum resolving power -- , make the Thomson backscattering technique very attractive.

On the other hand, the dependence of $d\sigma/d\Omega$ on the incidence angle is not as dramatic as the dependence on the scattered angle. Figure II.6 shows the dependence for $\beta = 0.80$, 0.85, and 0.90 respectively. The forward peak is the effect of the term in the large parenthesis in equation (II.11).

II-B-4 Classical derivation

To minimize algebra and to make the results clear for comparison with the QED expression, the scattering cross section is derived for a linear polarized plane wave scattered by an electron moving against the direction of wave propagation (figure II.7).

It is convenient to use the Lienard-Wiechert potential to evaluate the scattered fields (see Landau and Lifshitz ,1975)

$$\vec{E}_s = \frac{e}{c^2 R} \frac{\hat{k}_s \times \{ (\hat{k}_s - \vec{\beta}) \times \vec{a} \}}{[1 - (\vec{\beta} \cdot \hat{k}_s)]^3} , \qquad \vec{H}_s = \hat{k}_s \times \vec{E}_s \qquad (II.13)$$

where only far fields are kept in the expressions. R is the distance between the point of observation and the electron position, all the field quantities refer to the retarded time $t' =$
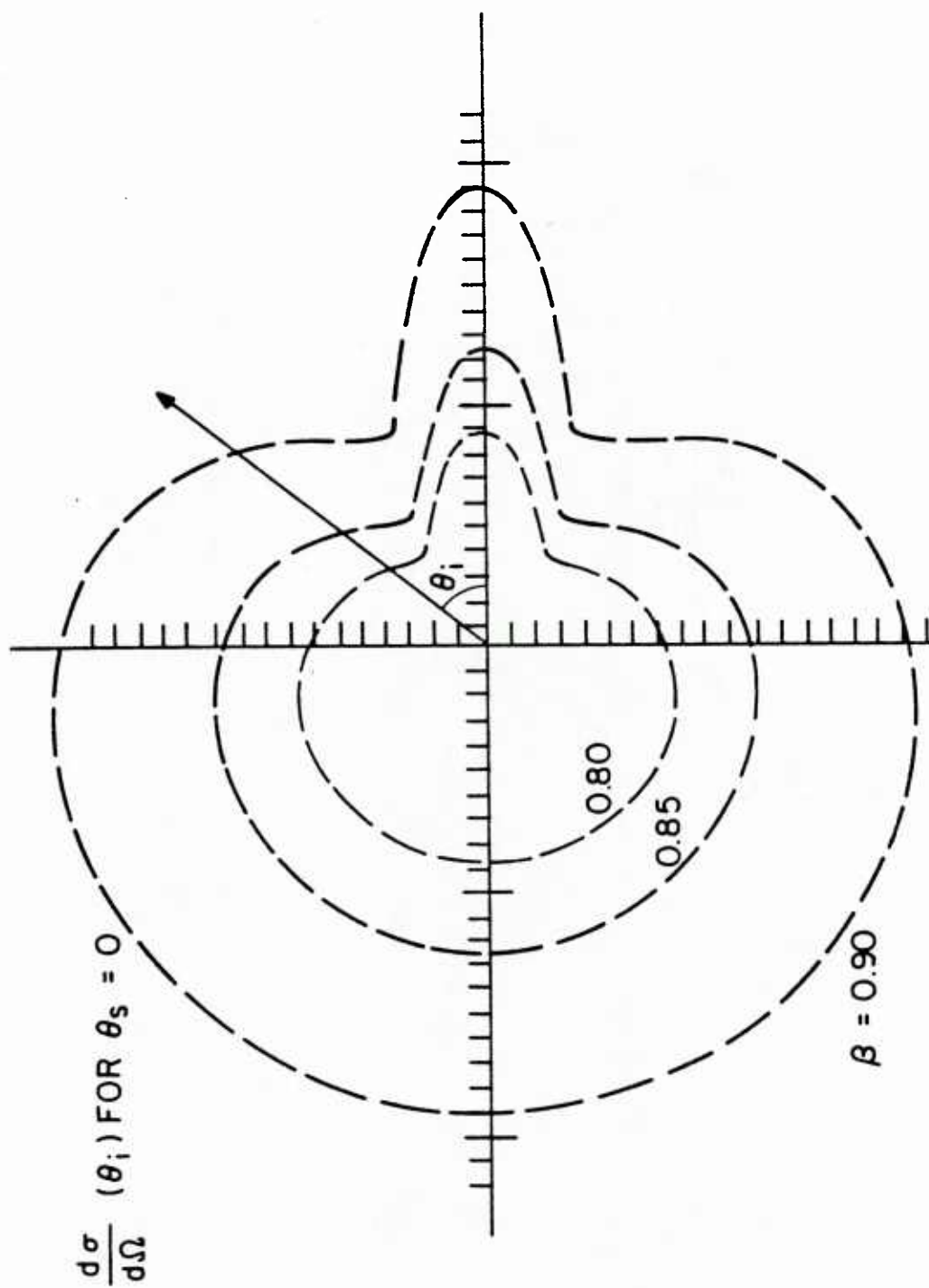
Figure II.6 Dependence of scattering cross section on incident angle for various electron velocities
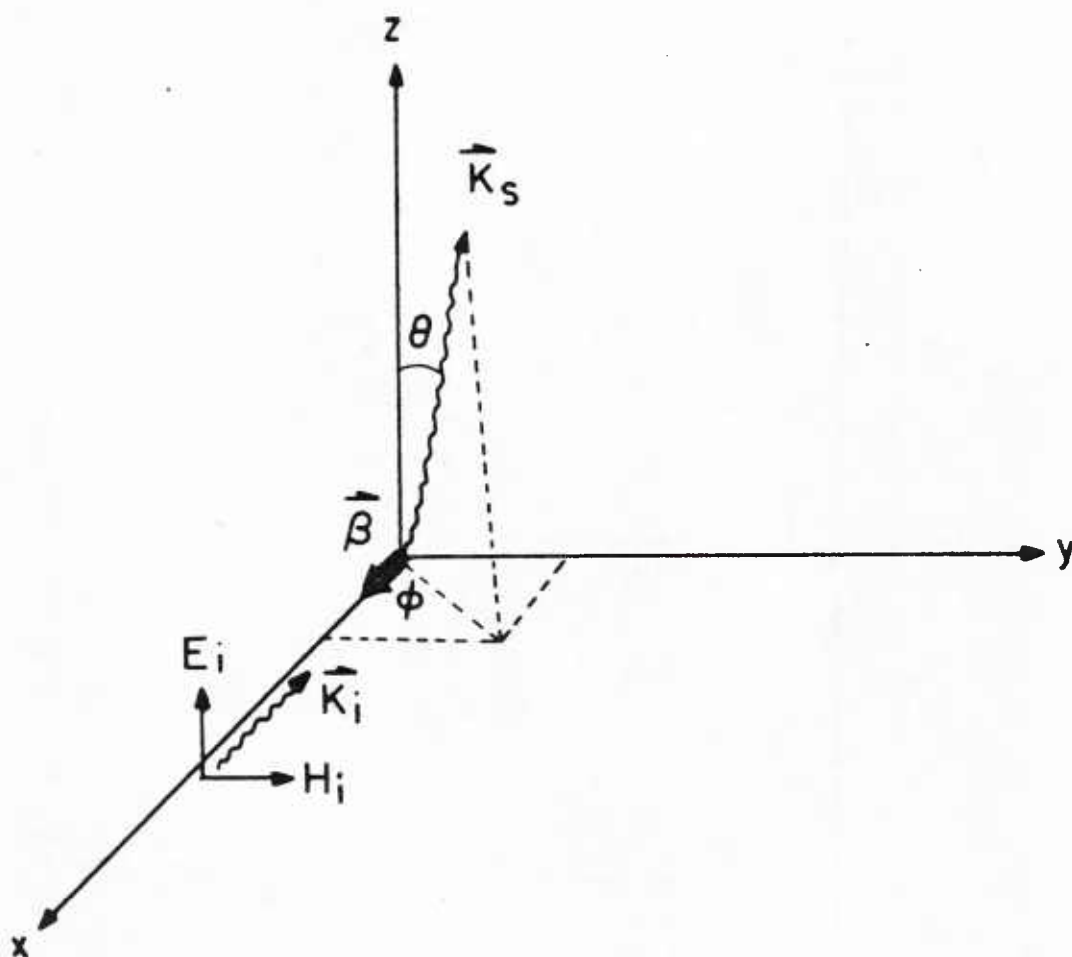
Figure II.7 Scattering geometry for classical calculation

t - (R/C).

The acceleration is calculated from the Lorentz force Equation

$$\vec{a} = \frac{e}{m\gamma} \left\{ \vec{E}_i + \vec{\beta} \times \vec{H}_i - \vec{\beta} \left(\vec{\beta} \cdot \vec{E}_i \right) \right\} \qquad (II.14)$$

The intensity radiated into the solid angle $d\Omega$ is

$$dI = \frac{c}{4\pi} \left| E_s \right|^2 R^2 \ d\Omega \qquad (II.15)$$

The energy differential cross section $d\sigma$ is the intensity dI normalized to the incident Poynting vector $\vec{S}_i$

$$d\sigma = \frac{dI}{|S_i|} = \frac{dI}{\frac{c}{4\pi} |E_i|^2} \qquad (II.16)$$

Inserting (II.14) into (II.13), and (II.13) into (II.15), and (II.15) into (II.16), we obtain the angular distribution of scattered power

$$\frac{d\sigma}{d\Omega} = \frac{\gamma_0^2 \ (1+\beta)^2}{\gamma^2 \ (1-\beta_s)^6} \left[(1-\beta_s)^2 - \frac{\cos^2\theta}{\gamma^2} \right] \qquad (II.17)$$

Three modifications should be made before comparing this expression with the QED result:

(1) Quantum Electrodynamic derivation deals with the probability of one photon scattered by one electron, the scattering cross section is a measure of the "scattered photon number". On the other hand, the classical derivation calculates the radiated power density, and is related to the "scattered photon

energy". To compare the classical expression on an equal footing with the quantum expression, the former has to be normalized to the photon energies, that is , multiplied by $(1 - \beta_s)/(1 - \beta_i)$.

(2) In equation (II.13), the quantities on the right hand side refer to the retarded time $t' = t - R/C$, while measurements are made in the lab at location R at the time t. A factor of $(1 - \beta_s)$ is needed in equation (II.17) to correct for the retarded time effect.

(3) Equation (II.17) is derived for incident radiation with polarization $\hat{e}$ in the $\hat{z}$ direction such that $\hat{K}_s \cdot \hat{e} = \cos \theta$. To average over all possible polarizations (say polarized at an angle α with respect to z axis), $\hat{K}_s \cdot \hat{e}$ is replaced by $\cos\theta \cos\alpha - \sin\theta \sin\phi \sin\alpha$, and integrated over α (0 to 2π) to get the unpolarized expression.

After making the above corrections, (II.17) becomes

$$\frac{d\sigma}{d\Omega} = \frac{r_0^2 (1-\beta_i)}{2\gamma^2(1-\beta_s)} \left\{ \left[1 - \frac{(1+\cos\theta)}{\gamma^2(1-\beta_s)(1-\beta_i)}\right]^2 + 1 \right\} \qquad (II.18)$$

which is in exact agreement with eq (II.11) when $\theta_i = \pi$.

II-C   Relation Between Beam Energy Spread and Scattered Spectum

The scattering experiment can be viewed from another useful point of view: with the incident radiation working as an electromagnetic pump wave on the electron beam, the whole device can be treated as an ill-designed free electron laser with an EM pump wave. In this case the undulator magnet, when energized, only plays the role of providing the perturbation for the electron velocity profile.

In the beam frame the Debye length is much longer than the Lorentz contracted "EM undulator" period $10 \mu m / 2\gamma$, so the interaction is non-collective, viz, in the single particle (Compton) regime. The calculated Compton gain for this "EM pumped" FEL of finite length is so low that the stimulated scattering process is negligiable and only the incoherent scattered radiation (i.e. the spontaneous radiation of electrons in the EM undulator) is observable. In other words, the bunching effects and the coherent gain processes do not contribute to the scattering signal.

A point should be made clear here: the "true" FEL interaction between the electron beam and the "magnetostatic undulator" is not observed in the experiment, although it is the actual mechanism responsible for gain and lasing. With the 700 KV beam energy and the 17 mm undulator period, both the spontaneous and the stimulated emission radiation are in the mm region, which does not interfere with the visible diagnostic signals.

The width of the spontaneous spectrum in a free electron laser is usually determined by the homogeneous broadening caused

by the finite undulator length effect $(\Delta\omega/\omega)_{homo} \sim 1/N$ and the inhomogeneous broadening of the finite temperature electron beam. In this experiment the number of "EM undulator" periods in the interaction region is more than 10^4, so the inhomogeneous broadenings dominate and are solely responsible for the line shape of the spontaneous spectrum. This means the spectral width of the scattered radiation carries the information of the electon velocity spread.(*)

The scattered spectrum is obtained by summing the contributions from all the electons over the velocity distribution incoherently using the single electron cross sections calculated in last section. For a cold beam, a realistic anzatz for the velocity profile in the beam frame is a narrow Gaussian. The integration over the electron velocity distribution is carried out in Zhuravlev and Petrov's paper (1979), which shows the specrum to be Gaussian provided the beam is cold enough. The width of the Gaussian is calculated to be

$$\left(\frac{\Delta\omega}{\omega}\right)_{inhomo} = 4\sqrt{\frac{2T_0}{m}\ln 2} \quad (FWHM) \qquad (II.19)$$

(*) On the other extreme, if the beam is cold enough, the spontaneous line shape is entirely determined by the undulator's wavelength Fourier component. This relation also has the potential of providing a useful diagnostic of electron trajectories and threshold behavior in FELs especially for the ones with tapered undulators.(See Bosco and Colson, 1983)

or in terms of energy spread in the lab frame

$$\left(\frac{\Delta\omega}{\omega}\right)_{inhomo} \cong 2\left(\frac{\delta\gamma}{\gamma}\right)_{\parallel} \qquad (FWHM)$$

(II.20)

this formula relates the spectral width to the electron energy spread. This expression is also obtained by differentiating equation (II.8) with respect to γ .

II-D   Remarks

The incoherent scattering of electromagnetic radiation by plasmas has attracted interests for a long time because of the possibility of exploiting this scattering to measure plasma properties such as the temperature and the magnetic field. Although the theory of scattering has been developed extensively, there have been interesting problems that are not settled until very recently -- the finite-residence-time effect and the polarization effect .

II-D-1   Finite-Residence-Time Effect

Pechacek and Trivelpiece (1967) were the first to study the finite-residence-time effect. This effect states that the expression for the intensity of the radiation scattered by a finite plasma volume differs from the corresponding expression for an infinite volume by an additional factor ($1 - \beta_S$) when it is to be integrated over the electron velocity distribution.

The simple verbal argument given in Pechacek and

Trivelpiece's paper is intuitively attractive but has serious flaws in it: the correction factor ($1 - \beta_S$) does not contain the volume parameter whose finite size it is supposed to incorporate. They interpreted the finite-volume-effect to be fundamental and not reducible to the infinite-volume case. This interpretation was propagated in several other papers.(*)

The attempt by Kukushkin (1981 a) to find an explanation for the missing of the volume parameter led him to the conclusion that the interpretation of the finite-volume-effect is a consequence of a mathematical error in Pechacek and trivelpiece's paper (1967), where they mishandled the square of a δ -function, which resulted in the missing of a factor ($1 - \beta_S$).

However, the finite time spent by the electron in the scattering volume should in principle change the incoherent scattering spectrum, though not according to the erroneous recipe ($1 - \beta_S$).

Kukushkin (1981 a) considered this effect carefully, and found that the true finite-residence-time effect of a particular electron in the scattering region appears as in a change in the broadening of the scattered line, while the change in the scattered intensity is ignorable, $\left(\Delta I / I\right) \sim \lambda_i/L$ (L is the system length) . The line broadening effect also turned out to be

---

(*) Nee, Pechacek, and Trivelpiece (1969); Sheffield (1972); Sheffield (1975); Ward, Pechacek, and Trivelpiece (1971); Ward and Pechacek (1972); Williamson and Clarke (1971); Zhuravlev and Petrov (1972); Zhuravlev and Petrov (1979).

very small in magnitude and undetectable in practical cases. This effect is suppressed accordingly as expected when the scattering volume approaches infinity.

Besides the finite-residence-time effect of the electrons, there should also in principle be a finite-pulse-length effect associated with the high power pulsed lasers used in the scattering experiments, especially for the case of mode-locked operation. Williamson and Clarke (1971) gave a suppression factor for the scattering cross section without derivation -- $\left(\frac{1 - \beta s}{1 - \beta_c} \right)$ This expression also turned out to be unjustifiable.

The short-pulse-length character of the laser is closely related to the finite-volume-effect , since both effects result in a finite longitudinal interaction length. The short-pulse-length effect is not appreciable as long as there are many wavelengths in one pulse (Kukushkin 1981 a).

II-D-2   Polarization Effect

Another important question is the mutual consistency of the classical and the quantum electrodynamic scattering cross sections for any combination of photon polarizations. There has been some citations back and forth in the literature, but these two expressions have not been compared in a rigorous way.

For most of the expressions given in the literature, the Stokes parameters of the photons are defined with respect to the electron velocity directly or indirectly. This results in neat-looking equations that are not suitable for direct averaging over

the electron velocity distribution. These expressions also make it impossible to make comparisons with classical results.

A more rigorous derivation of equations for the scattering process was given in Kukushkin's paper (1981 b). By transforming to the new Stokes parameter space determined with respect to unit vectors which do not depend on the electron velocity, he demonstrated that the classical and the quantum cross sections are consistent in general.

Chapter III

EXPERIMENTAL APPARATUS

III-A   Introduction

The following sections describe the major components of the scattering experiment. Figure III.1 shows the four subsystems involved . Section B describes the two stage TEA CO_2 laser system that provides a high power infrared beam; the related optics is also discussed. An overview of the Marx generator and the pulse line technique, followed by a description of the plasma-induced field-emission diode configuration that generates the cold electron beam , is presented in section C.

Section D deals with the magnetostatic undulator , an integral component of an FEL. This is used to study the axial energy spread inhomogeneous broadening induced by the radially-dependent pumping field , $\vec{B}_{\perp}(r)$. The final section describes the optical system and detector utilized to extract spectral information from the radiation scattered by the electron beam.
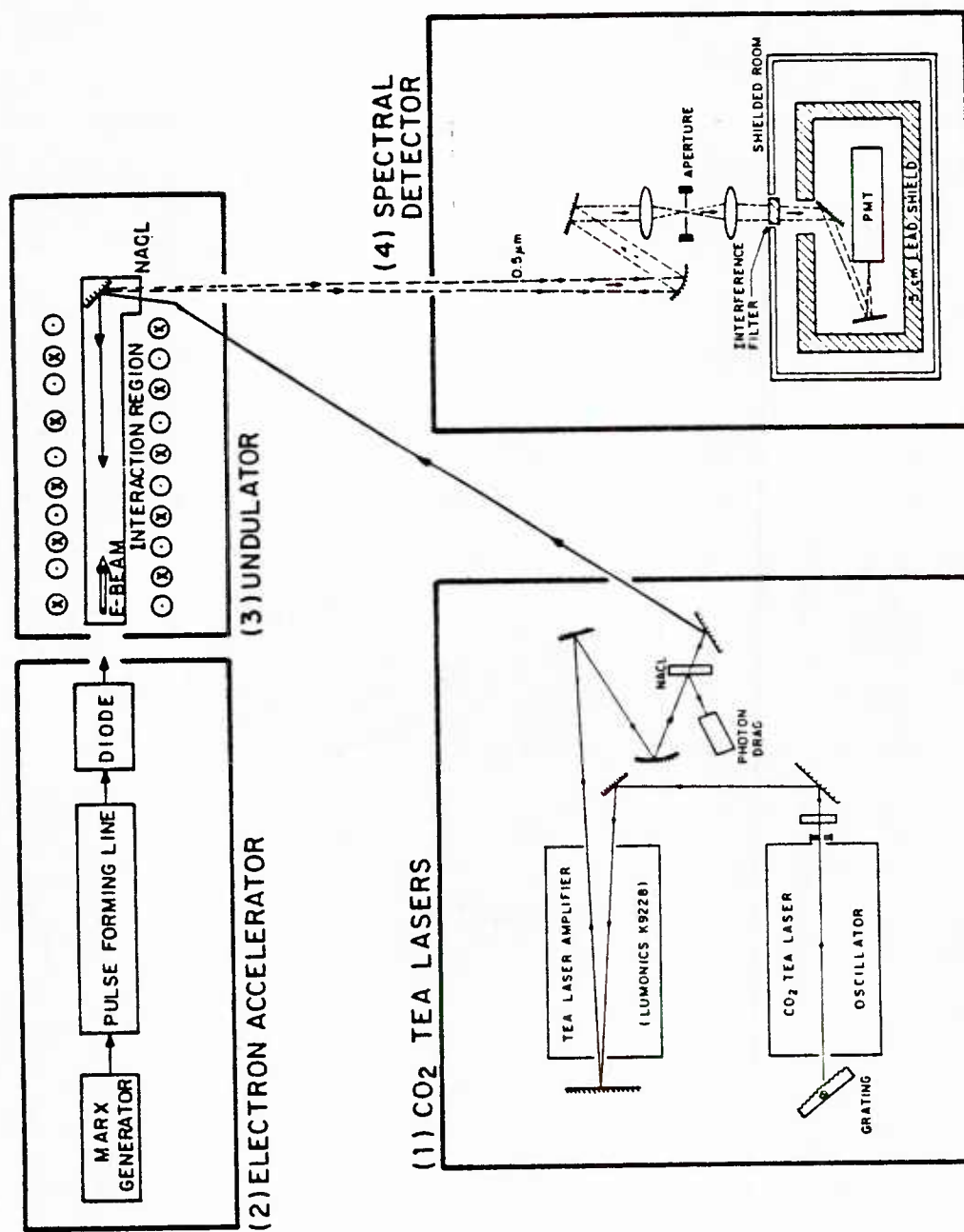
Figure III.1 Four major components of the experiment

III-B   CO$_2$ Laser System

III-B-1   Principles of Operation

The laser system consists of a "homemade" CO2 laser oscillator and a Lumonics 922S laser amplifier (Figure III.2). These two TEA lasers operate by the method of transverse electrical excitation of a lasing gas mixture, this allows a large amount of energy to be dumped into a gas at atmospheric pressure at resonable voltage levels.

A uniform plasma is formed in the laser cavity when the atmospheric pressure gas mixture is subjected to a high current density. The energy of the electrons (a few eV) in the plasma is utilized to excite the gas molecules to some vibrational levels. For TEA lasers using a nitrogen, helium, and CO2 mixture, the population inversion builds up either by direct exitation of CO2 upper lasing level, or by resonant transfer of energy from the excited nitrogen molecule to the CO2 upper lasing state (Figure III.3). Helium plays the role of de-exciting the lower lasing state through collissional relaxation to ground state.

The two TEA lasers are each made up of two identical modules connected in series. The schematic is shown in figure III.4. In each section, an energy storage capacitor (0.1 μF) is charged to a preset voltage. By triggering the spark gap switch, energy is released to the main discharge electrodes to pump the gases. Paralleling these electrodes is a series of preionizing spark gaps. Each one is energy-limited by a small capacitor (500 or 920x2 pf) in series. These small gaps see the same voltage

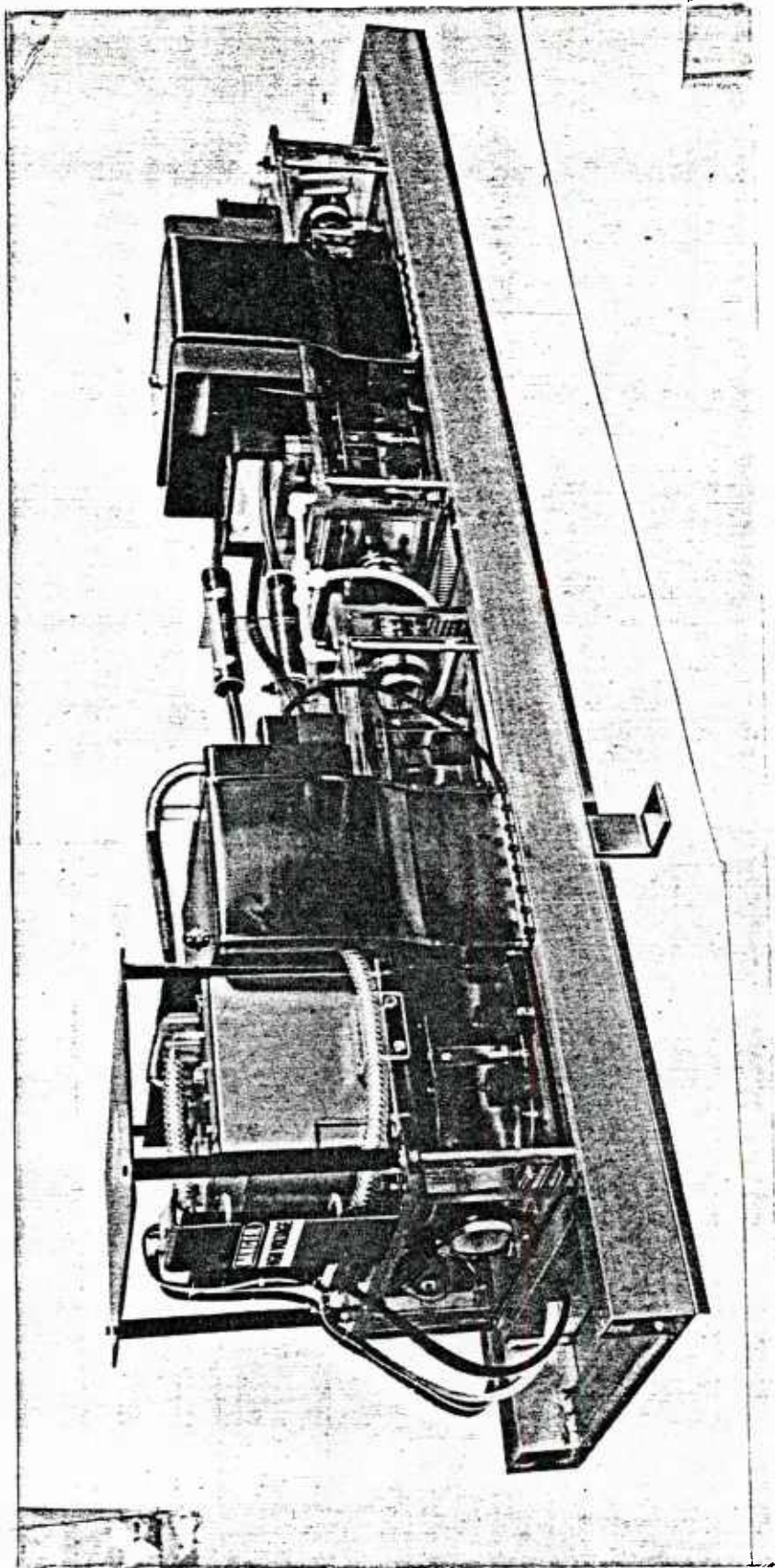Figure III.2 Lumonics K-922S CO_2 TEA laser
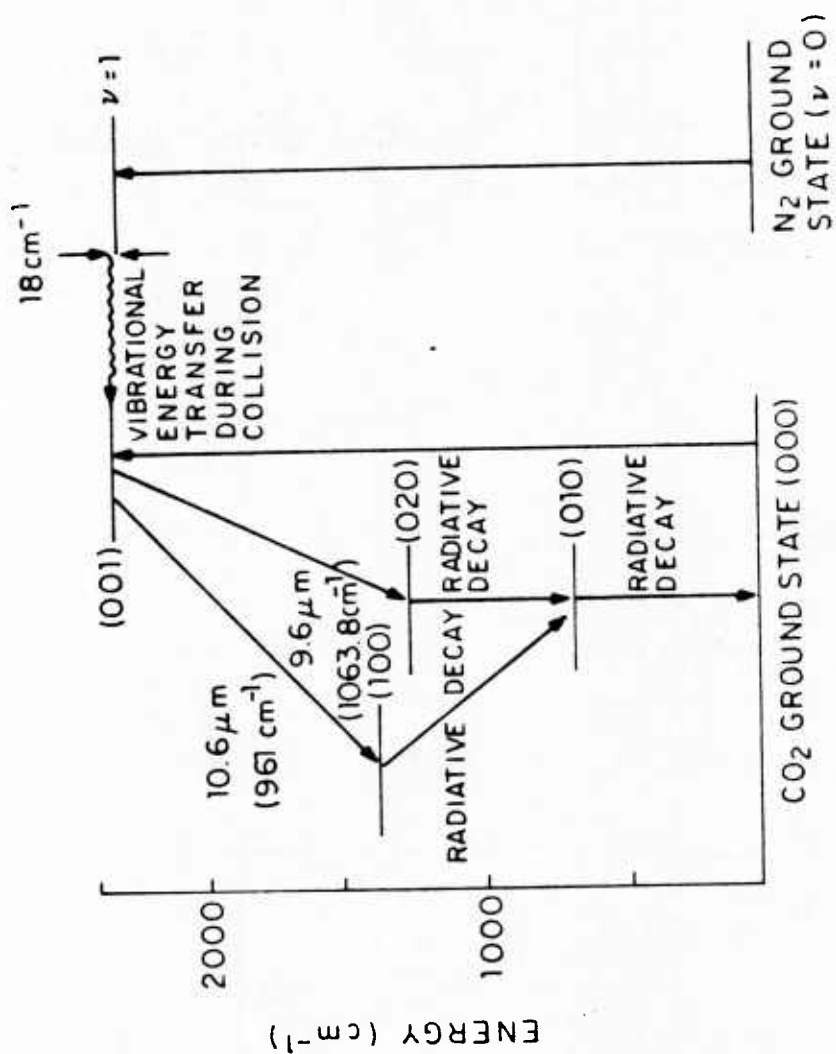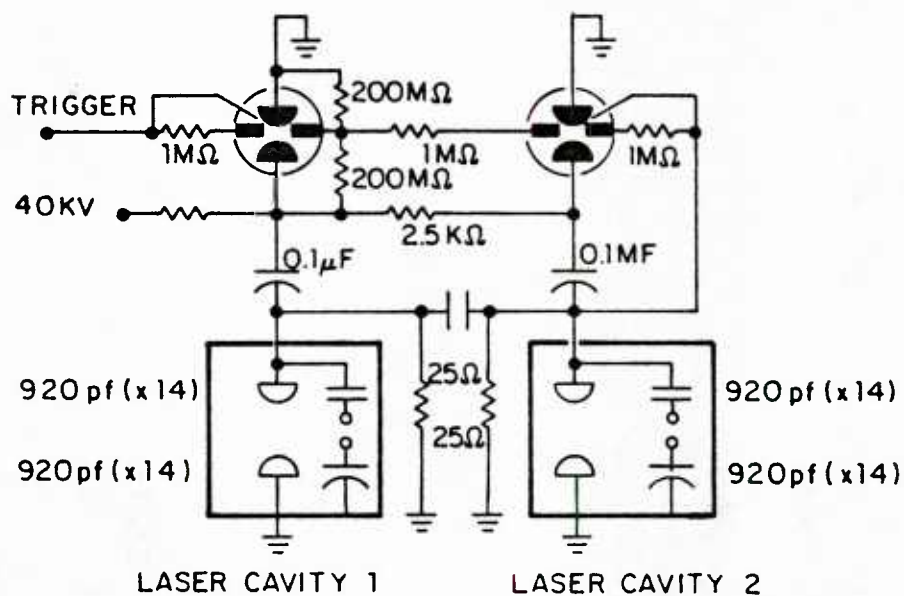
47

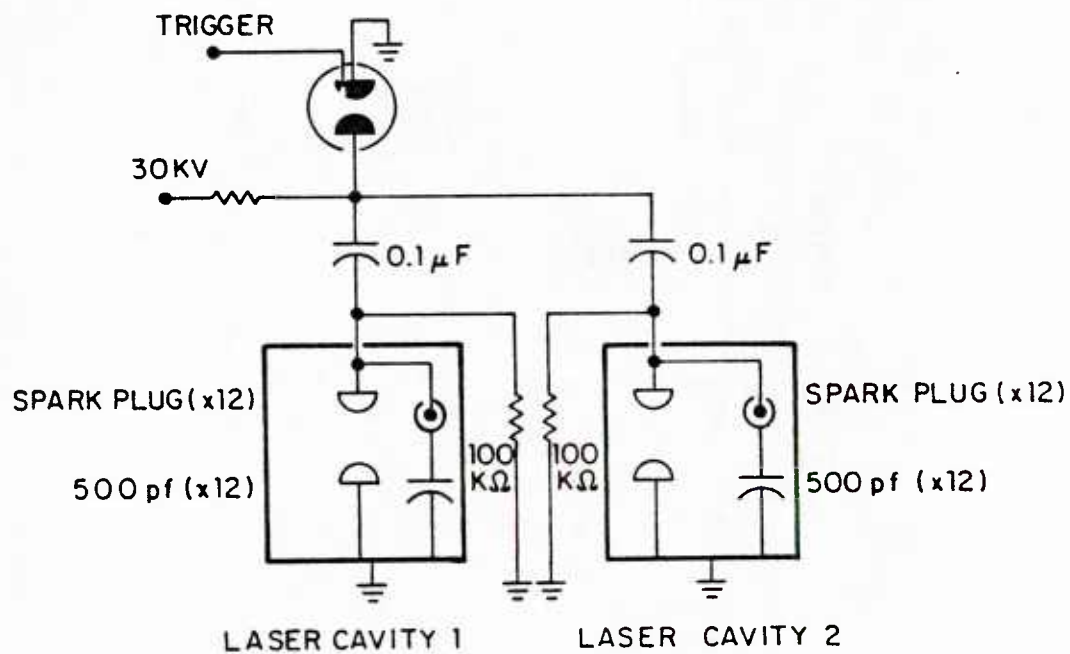Figure III.3 Vibrational levels involved in the operation of CO₂ lasers

(a)

(b)

Figure III.4 (a) Lumonics CO_2 laser amplifier schematic
(b) Homemade CO_2 laser oscillator schematic

pulse as the main electrodes, and will break down first to provide a uniform preionization for the main current pulse.

The oscillator and amplifier laser are similar except the following minor differences: (1) Two midplane type switches work in parallel to discharge the corresponding storage capacitor in the amplifier ; only one trigatron type switch is used in the oscillator to fire both sections. (2) Regular automobile spark plugs are used as the preionizing discharge gaps in the oscillator, whereas the amplifier makes convenient use of the metal screws on the capacitors as electrodes. (3) Different operating voltage and cavity size of these two lasers lead to different requirements for the gas mixture and flow rate.

III-B-2   Laser System Layout

The oscillator is tuned to the 9.6 μm P(24) line of the 001-020 band by a diffraction grating acting as a mirror. An intracavity diaphragm is used in the oscillator to suppress off-axis modes (Figure III.5). A partial transmitting ZnSe mirror is used as the output window on the other end . The length of the osillator cavity is 300 cm. The round trip time 2L/C defines the spacing between successive mode-locked spikes which is 20 ns. The output is double-passed through the amplifier laser which is timed to amplify the 120 ns pulse.

The TEA lasers are triggered by sending high voltage pulses to distort the high voltage equilibrium field in the pressurized
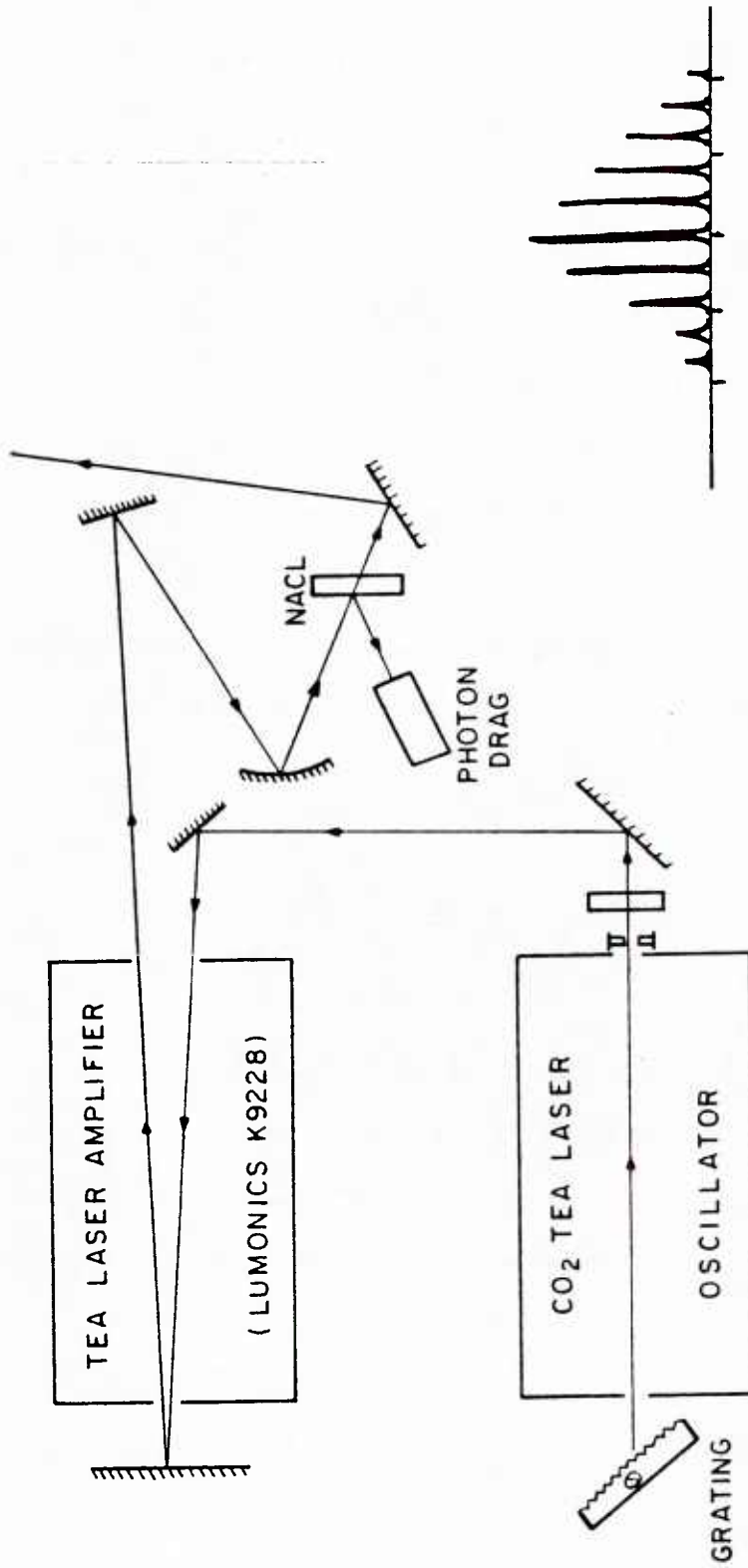
Figure III.6 CO_2 laser output
waveform (50 ns/Div)
(50 ns/Div)

Figure III.5 Incident CO_2
laser system and optics

spark gaps, and closing the gas swithes . The laser build-up time, that is, the time lag between the breakdown of the oscillator spark gap and the actual lasing, is sensitive to the spark gap pressure, operating voltage, and especially the gas mixture in the laser cavity. With a 25:6:2 ratio of He:CO2:N2, fired at 30 KV, and with 15 lb of CO2 pressure in the switch, the time lag is 1.18 μs. To minimize the time jitter introduced by the switch, the gas pressure should be just a few pounds above the self-fire limit.

The trigger to the amplifier spark gap is delayed for about 500ns to compensate for the shorter build-up time of the amplifier laser. Once turned on, the amplifying gas mixture remains active for more than 1 us. The oscillator output is easily captured and amplified.

However, the 50 ns jitter associated with the CO2 pulse causes a problem in synchronizing with the electron beam pulse, which is also controlled by SF_6 gas switches with a typical jitter of 40 ns.

The amplifier output is directed into the interaction region through a NaCl window. The high power density of the output makes it necessary to place the first mirror at least 3 meters away from the amplifier laser output window. The amplified radiation (2x3 cm^2) is focused by a 5 meter focal length mirror down to a 6 mm diameter spot, about the same size of the electron beam cross section. A focusing optics of f/120 is employed so that the radiation is scattered efficiently by the large aspect ratio electron beam. Copper mirrors are used as the last two optical components in directing this high power density beam into

the scattering region.

The laser power is monitored with a photon drag detector, which detects the radiation (about 5 % of the total power) reflected off a NaCl flat located in the optical path. The laser system provides about 20 MW of power in a sequence of mode-locked narrow spikes, about 20 ns apart, spaced over a 120 ns interval (Figure III.6). These equally spaced spikes make a convenient signature for identifying the scattered signal.

III-C   The Electron Beam

III-C-1   Electron Accelerator

The accelerator (Physics International 220G) consists of a Marx generator, a pulse forming line, and an impedence matching radial resistor (Figure III.7). A schematic showing the principle of operation is shown in figure III.8. The Marx generator is charged to a preset voltage by a DC power supply, then a fast-rising trigger pulse erects the Marx and charges the pulse forming line. The output switch will close in due course, and the charge is transferred through the radial resistor to the diode region. The output switch prevents voltage from appearing on the cathode before closure.

The Marx generator has twenty 0.118 μF energy storage capacitors immersed in oil. A simplified schematic of this circuit is shown in figure III.9. These capacitors are charged in parallel to a desired level . When the SF6 filled spark gap
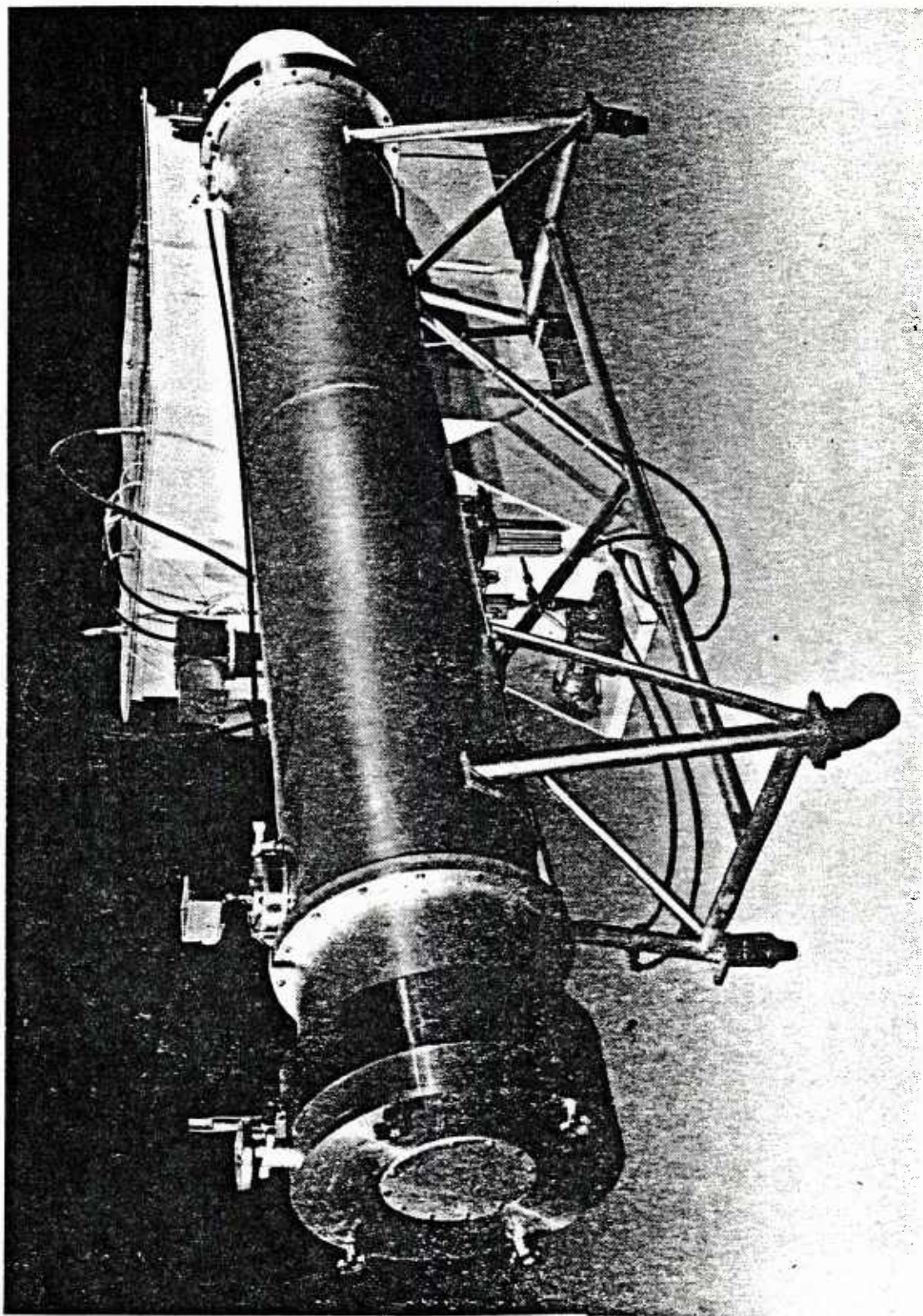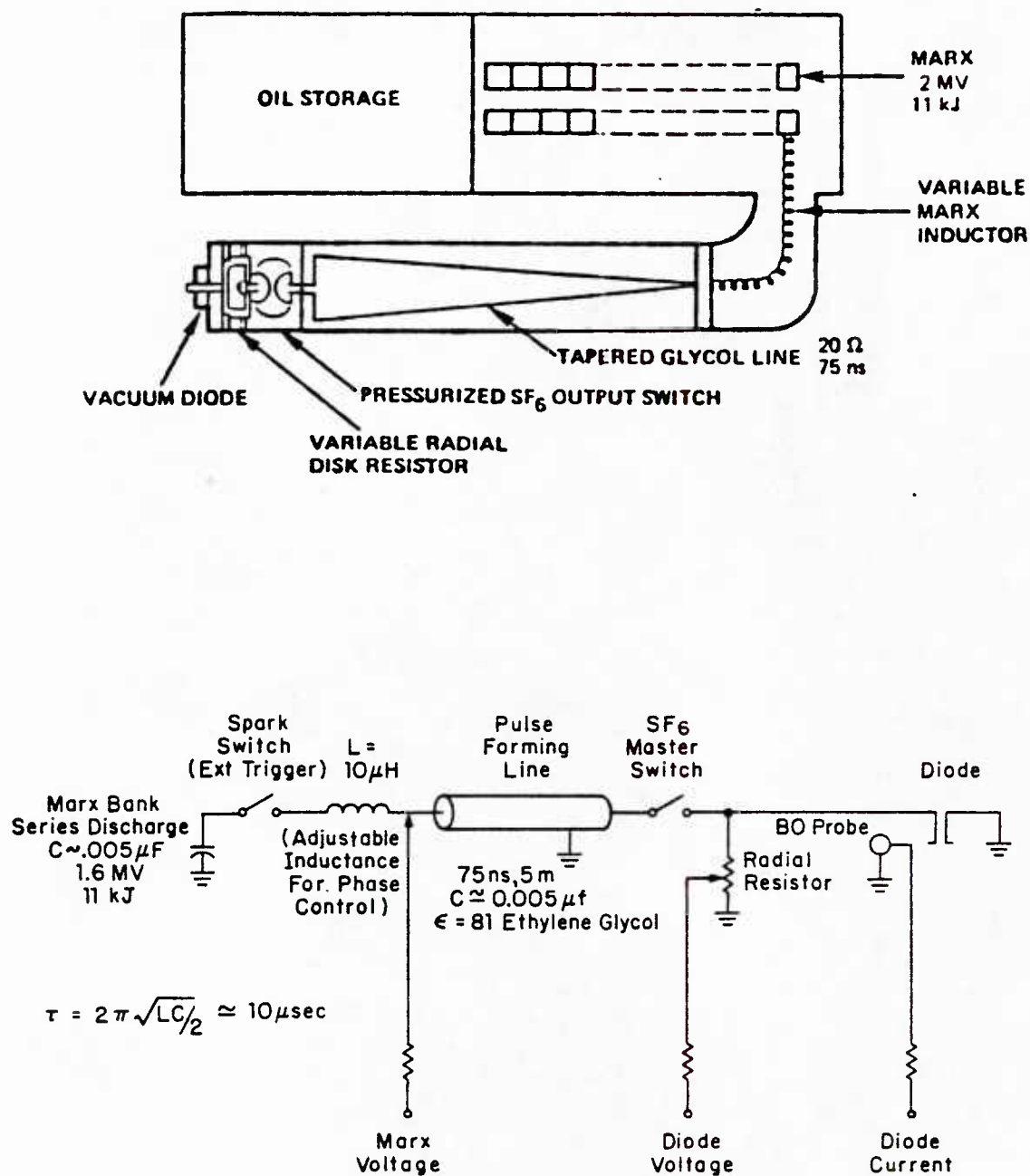
Figure III.7   Electron accelerator
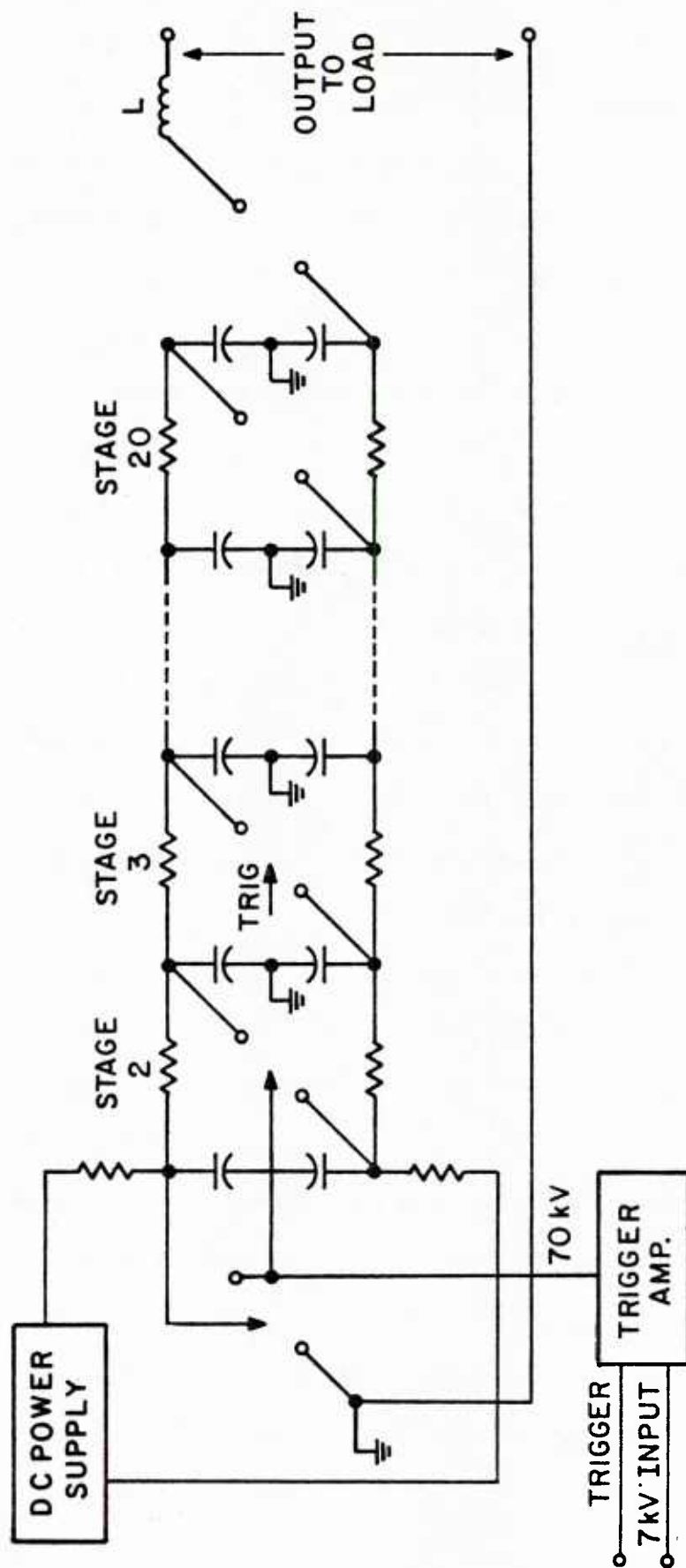
Figure III.8 Accelerator schematic

55

Figure III.9 Marx generator schematic

switches are triggered, the capacitors are connected in series, so the output voltage of the geneator is 20 times the charging voltage. Each capacitor is shunted by isolation resistors. The time constants are adjusted so that only a few percent of the stored energy is dissipated in these resistors.

Because the internal inductance of Marx generator may limit the rate of current rise in the load, the generator output is used to charge a coaxial transmission line, which in turn drives the vacuum diode. It can be seen from figure III.8 that this circuit is equivalent to the underdamped series RLC circuit and produces a ringing waveform with a characteristic frequency ($w = \frac{1}{2} \pi \sqrt{LC}$) greater than that of the Marx alone, because the line's capacitance nearly equals that of the Marx generator. When the waveform reaches its first maximum, an untriggered pressurized SF6 switch breaks down and connects the line to the diode and the radial resistor.

The Marx voltage and the diode voltage are monitored with CuSO4 solution dividing resistors. The voltage monitors are carefully calibrated as follows: An external capacitor bank with low inductance is charged to a known high voltage (measured with great precision with an electrostatic high voltage meter). Then a switch is closed to apply the voltage across the load (the radial resistor and the diode in parallel). The output waveform is measured by exactly the same circuit elements (same cables, connectors, external attenuations) as the ones used in monitoring the Marx or diode voltage. So the calibration factor is determined accurately through a "black-box" method without knowing the exact parameters of the various circuit elements

involved.

Figure III.10(a) shows the Marx output voltage which is applied to the transmission line. Figure III.10(b) shows the voltage that is applied to the vacuum diode at the output of the master switch. The Marx voltage shows a stepped waveform component superimposed on the 1-coswt charging waveform. This occurs because the PFL has a larger impedence than the Marx generator inductor, so reflections arise from the mismatch of impedences.

The Marx impedence must be adjusted so that the peak of the 1-coswt waveform coincides with a charging step, and a flat voltage pulse may be produced at the diode. The diode switch must break down just before this flat peak, which is accomplished by adjusting the SF6 pressure.

As the pressure in the output switch is increased, the voltage required for breakdown is increased and switching is delayed relative to charging voltage. If the pressure is too high, the voltage needed for breakdown exceeds the voltage that can be supplied by the PFL. In this case, the energy is reflected back into the line, and voltage reversal, followed by breakdown in the dielectric, occurs. Part of the energy goes into acoustic waves, a situation which is to be avoided at high energies.

In order to match the impedence of the PFL with that of the diode, an adjustable radial resistor is placed in parallel with the diode. The resistor consists of a five-gallon volume of sodium-thiosulfate solution located between the output switch and the vacuum diode. The resistance may be adjusted by changing the
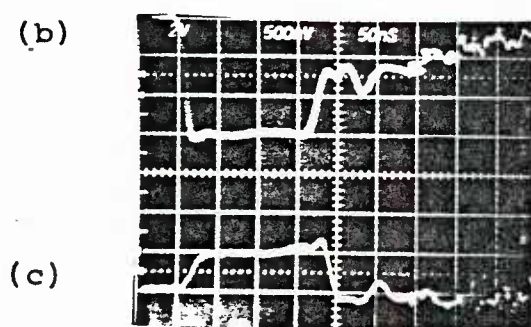
(b)

(a)

(b)

(c)
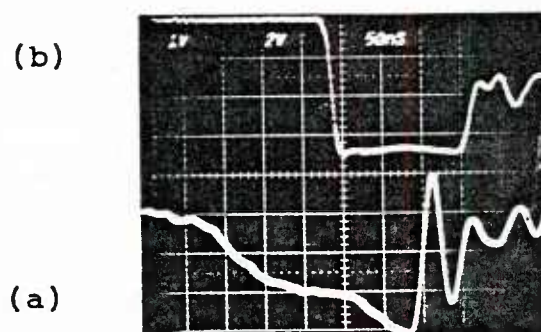
Figure III.10 (a) Marx output voltage, 300 KV/div, 50 ns/div
             (b) Diode Voltage, 200 KV/div, 50 ns/div
             (c) Diode current, 5 KA/DIV, 50 ns/div

concentration of the solution. The conductivity is measured to be 180 umho. The impedence of the diode decreases about 10% during the firing phase. This can be seen from the increase in the diode current (Figure III.10(c)). The radial resistor works as an effective ballast, making the voltage drop appeciably smaller (2% for 50 Ω diode). To further compensate for this impedence collapse, the center conductor of the PFL is mounted on an eccentric cam. This enable the coax line to be moved off center, which reduce the effective taper of the line. This effectively changes the impedence of the line so that the output voltage can be ramped up to 4%, thereby compensating for diode impedence collapse.

III-C-2   Vacuum Diode

For cold cathode diodes typically used in free electron laser experiments, the emittance of the generated beam is very sensitive to the diode geometry. To meet the cold beam requirement set by the Ramam free electron laser, the diode has to be designed specially.

The diode configuration used in this experiment is adopted from the NRL design (Jackson et al., 1983). The electrode surfaces are shaped to provide a radial electric field to balance the self-pinching effects of the azimuthal magnetic field. It turns out that the the cathodic electric fields are too high to control the emitting surface, and it is necessary to use only the central part of the beam (10% of the current); the other 90% is collected by the anode. Using only the cold, near-axis portion of

the beam , the computational analysis showed the beam axial velocity spread is expected to be smaller than 0.1%, which corresponds to a normalized total beam emittance of 30 π mrad.cm, and an energy spread $\leq$ 1 % .

The diode geometry, as well as equipotential contours and electron trajectories under typical guiding field and diode voltage, are shown in figure III.11. In this design, the cathode is a graphite cylinder with a hemispherical tip. To keep the emitting surface small and the diode impedence high, the cathode tip has a radius of curvature of 2.5 cm on the face and 0.5 cm on the edge. The anode is a graphite disk with a 15° conical concave surface and a 5 mm diameter aperture on axis. The gap between cathode and anode is 1.5 cm in our experiment: this avoids occational short circuits during the diode voltage pulse.

The whole diode assembly is immersed in a guiding field of 9.5 KG (Figure III.12). The apertured electron beam propagates on the axis of a 71cm long, 1.9 cm i.d. stainless drift tube . The upstream pressure in the interaction region is in the range 10^{-4} to 10^{-5} Torr.

III-D   The Undulator

A current driven helical conductor provides a right-hand-circularly-polarized magnetostatic field to interact with the electron beam. This bifilar helix consists of two coils of copper wire wound on a grooved nylon form. The undulator is 43 cm long and contains 25 periods of oscillation (1.7 mm period). A 3-

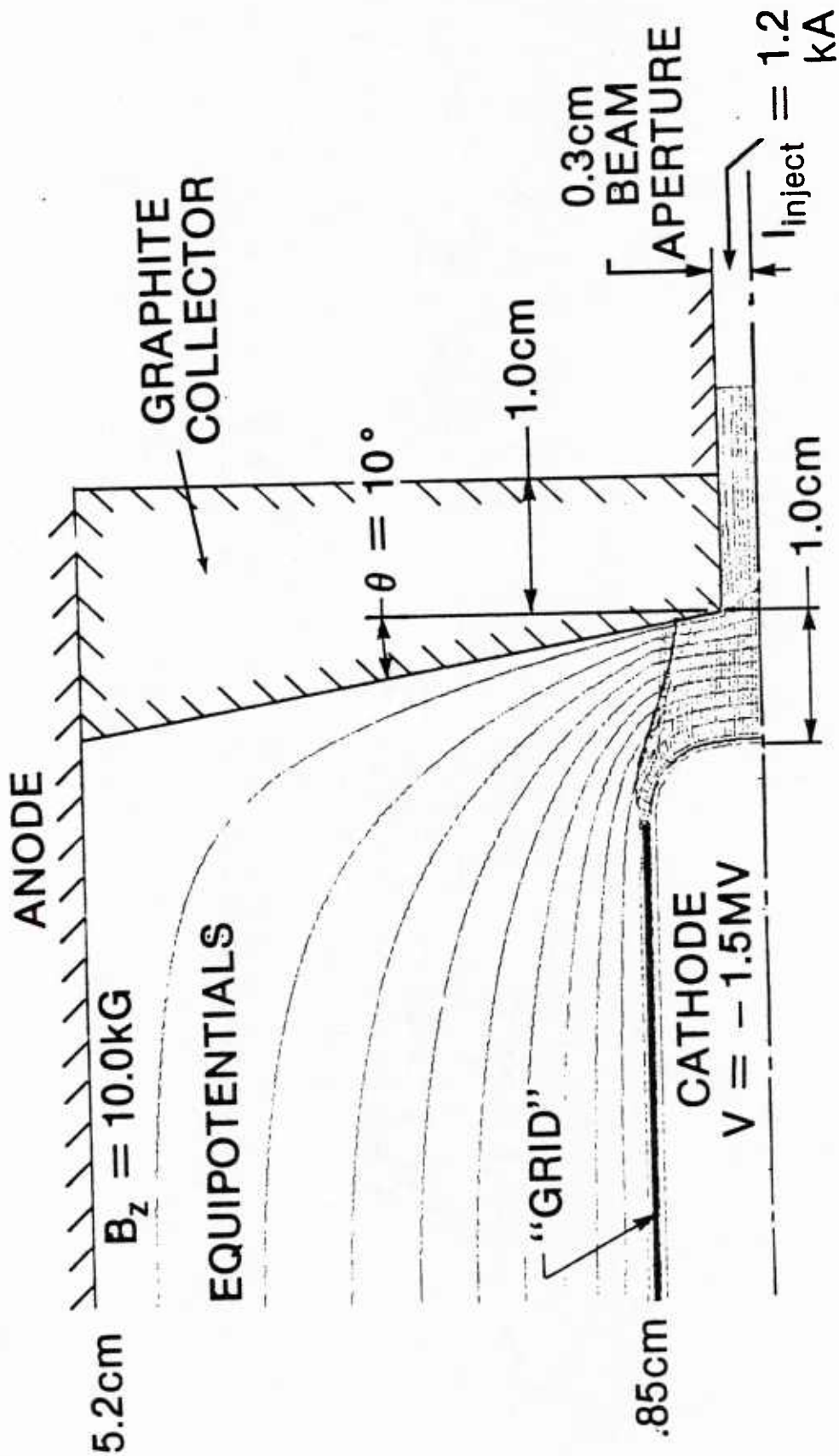Figure III.11   Vacuum diode geometry   (After Jackson et al., 1983)
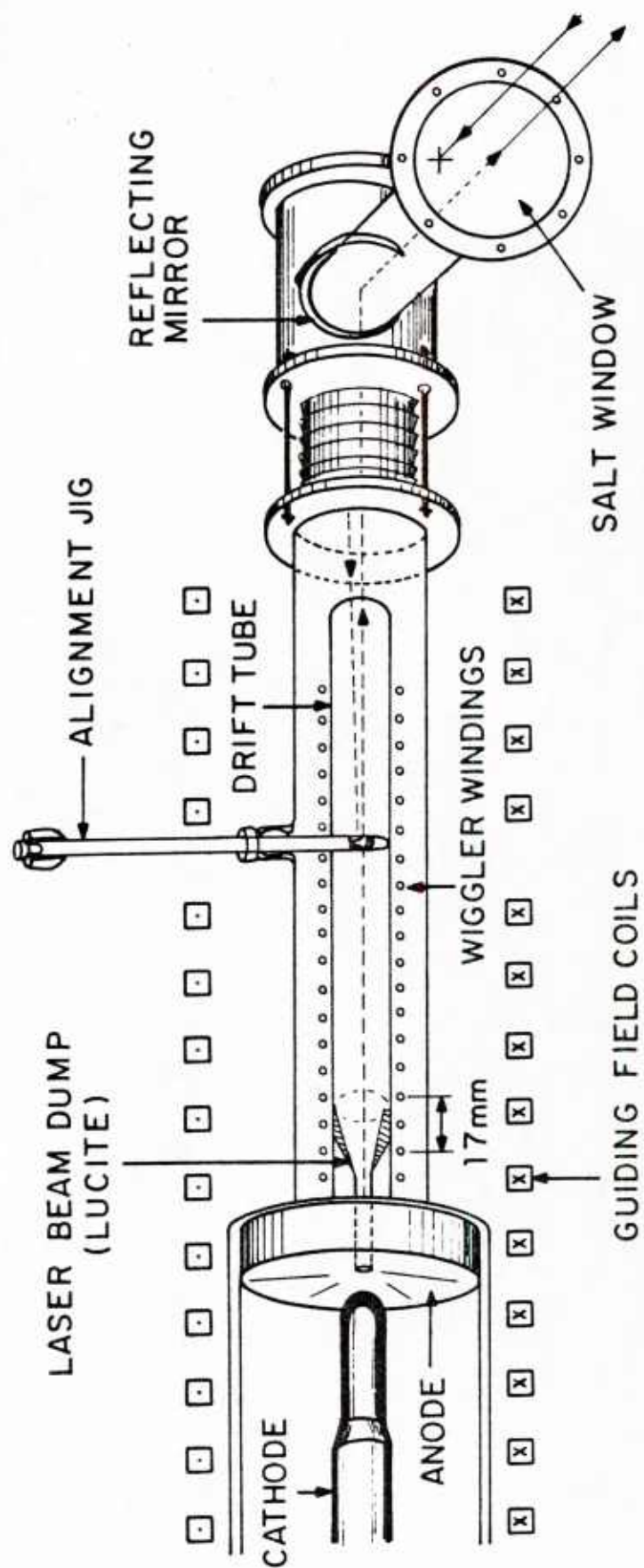
Figure III.12   Diagram of scattering region

CATHODE

ANODE

LASER BEAM DUMP
(LUCITE)

ALIGNMENT JIG

DRIFT TUBE

17mm

WIGGLER WINDINGS

GUIDING FIELD COILS

REFLECTING
MIRROR

SALT WINDOW

period transition region is introduced on both ends of the undulator by a gradual increase of the radius of the winding to prevent strong perturbation of the beam. The transverse undulator field is variable from 0 to 600 Gauss by adjusting the charging voltage of the capacitor bank which energizes the coils.

The transverse field intensity is measured with a standard pickup coil. A multi-turn current loop with diameter smaller than the undulator period is used so that the oscillation of the transverse magnetic field along the longitudinal direction can be resolved. When the undulator is pulsed, the output waveform of the field probe measures the induced current in the probe ,which is proportional to $\dot{B}_{\perp}(t)$.

The probe is calibrated by measuring the field intensity of a pair of Helmholtz coils (with known Gauss/Ampere) energized by the same capacitor bank through the same Thyratron pulser. A Rogowski coil is used to determine the current and also the field intensity in the Helmholtz coils. The induced current picked up by the probe is integrated once to obtain a quantity proportional to the field, which gives the probe calibration factor.

III-E   Spectral Detector

The scattered 0.5 μm light from the interaction region is collected by a 103 cm focal length mirror. This corresponds to a f/30 optical system. The collected light is focused further by a lens (25 cm f.l.) down to a 1 mm spot where an aperture stop is used to reduce the visible light pickup from the diode and the

TEA laser beam dump (Figure III.13). Aperture size is optimized to increase the signal to noise ratio by a factor of 3. After passing through the aperture, the diverging beam is focused again and directed into a shielded room through a 1 inch window in the wall, and into a copper box, which is enclosed in a wall of lead 5 cm thick.

A RCA C31000A photomultiplier tube in a 3 cm thick lead jacket is located in the copper box. The quantum efficiency of the multialkali photocathode is 11 % at 5000 $\overset{\circ}{A}$. A current gain of $\sim 10^{7}$ is expected at 2.5 KV tube voltage. The fast anode pulse rise time makes it possible to detect the sharp scattered spikes. Spectral information is obtained by filtering the scattered light with a set interchangeable interference filters, whose transmission peaks are at 5000 $\overset{\circ}{A}$, and with various bandwidths: 50, 80, 100, 200, 250, 500 FWHM in $\overset{\circ}{A}$. These filters fit into the 1 inch window in the shielded room. The effect of non-ideal (non-Gaussian) transmission filters on the interpretation of scattering results will be discussed in section IV-D.
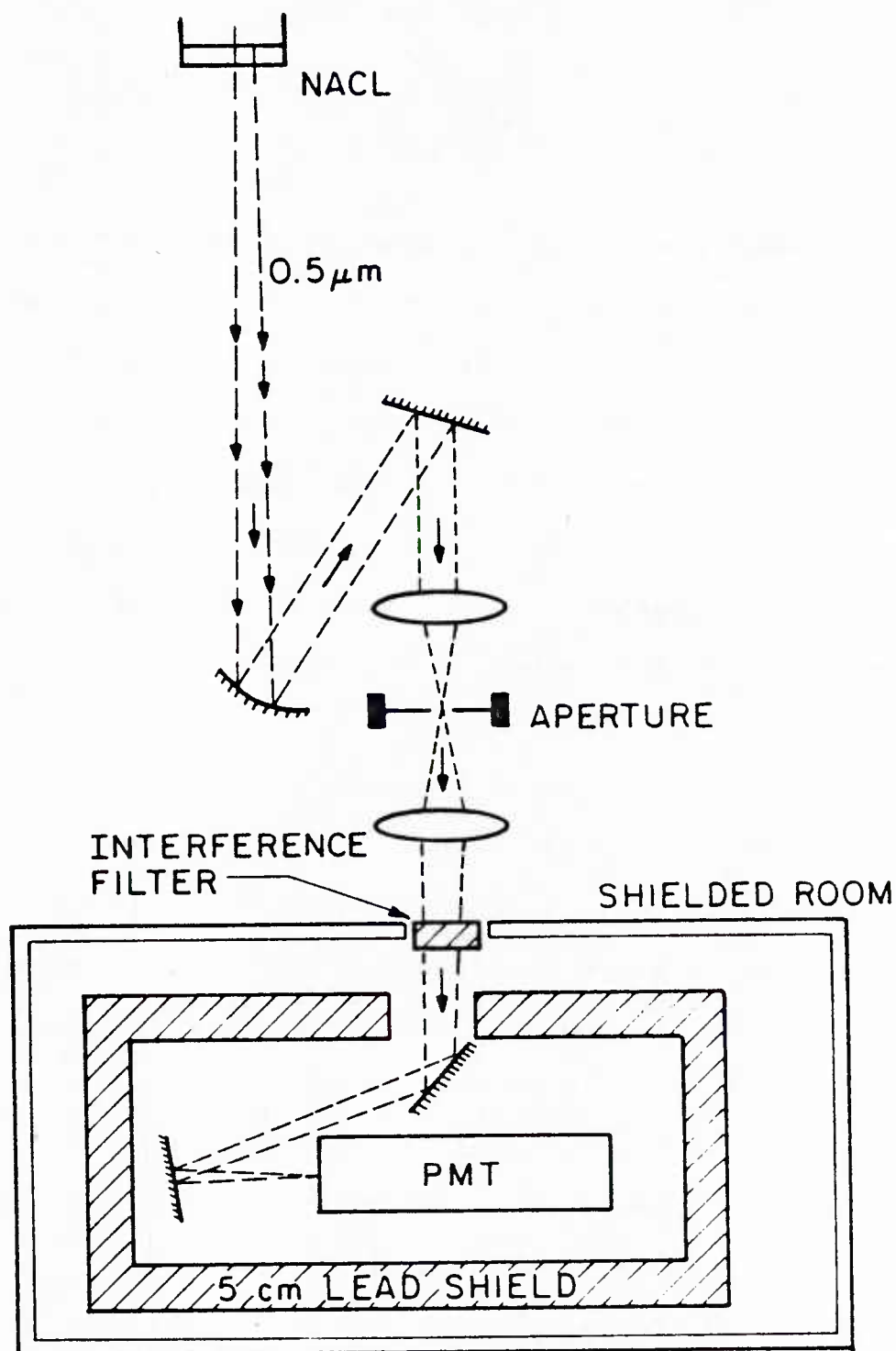
Figure III.13 Layout of scattered beam line optics
and detector system

Chapter IV

EXPERIMENTAL METHODS

IV-A   Introduction

A common problem in all Thomson scattering experiments is
the small interaction cross section.   Although we gain an
enhancement factor of $4\gamma^2$ from the relativistic electron beam,
the particle density is lower than typical plasma scattering
experiments by one to two orders of magnitude. The relatively
high noise background has to be brought down to a reasonable
level. Design considerations to maximize signal intensity and
techniques used to reduce noise generation and pickup are
described in section IV-B.

The   long focal length optical systems employed in both the
incident and scattered beam lines cause difficulties   in
alignment. The   short-pulse character of the electron and laser
beam make the relative timing a critical issue. Details of the
alignment and the timing scheme are described in section IV-C.

Section IV-D explains how spectral information is extracted
from the single channel data. Complications from "non-ideal"
transmission characteristics of the filters are solved by a map-
matching procedure developed for this purpose.

Since the diode region needs routine cleaning, the maximum
number of shots that can be fired in one day is limited to 30.
This makes data acquisition a time-consuming process and day-to-
day optical realignment a necessity.   However, this is an
intrinsic difficulty that cannot be removed.

IV-B   Signal-to-Noise Ratio (S/N) of the Experiment

IV-B-1   Preliminary Considerations

The velocity profile in one direction is most efficiently studied by observing light scattered along that direction (Section II-B-2). So $\hat{K}s$ is chosen to be parallel to $\vec{\beta}$ in the scattered spectrum formula

$$\frac{\omega_s}{\omega_i} = \frac{1 - \vec{\beta} \cdot \hat{K}_i}{1 - \vec{\beta} \cdot \hat{K}_s} \qquad (IV.1)$$

To maximize frequency upshift and scattering cross section, the incident wave vector $\hat{K}i$ is made antiparallel to the electron beam direction. This geometry provides an upshift factor of 19.2 for a $\gamma = 2.3$ electron beam.

The CO_2 laser is chosen as the photon source not only because it operates with high power and efficiency, but also because the 9.6 μm incident radiation is backscattered into the visible part of the spectrum (0.5 μm) where detectors are most sensitive.

IV-B-2   Spectral Resolution

The scattered spectral width and the beam parallel energy spread is related linearly by

$$\left(\frac{\Delta\omega}{\omega}\right)_{inhomo} = \frac{2}{\beta}\left(\frac{\Delta\gamma}{\gamma}\right)_{/\!/} \qquad (IV.2)$$

To detect an energy spread of 1-2 % with accuracy, we need a

diagnostic capable of resolving a $(\Delta w/w)_\Omega$ of 0.1 %. In comparison, the linewidth of the 9.6 μm transition in CO2 TEA lasers is about $(\Delta w/w)_{CO_2} = 0.001\%$ (*), and is monochromatic enough for this purpose.

The main constraint on the resolving power comes from taking measurements on an angular dependent spectrum by collecting radiation in a finite solid angle $d\Omega \cong \pi (d\theta_s)^2$. Equation (II.9) shows the second order angular broadening at zero observation angle. In this experiment, the output beam line is tilted at a small angle ($\sim 1^\circ$) to minimize noise pickup (Section IV-B-4). A more pertinent equation is obtained by differentiating equation II.8 with respect to θ_s, when $\theta_s \rightarrow 0$; we get

$$\left(\frac{\Delta w}{w}\right)_\Omega \cong -2\gamma^2 \theta_s (\Delta\theta_s)$$

By increasing $d\Omega$, we gain in signal level at the expense of spectral resolution. To achieve a $(\Delta w/w)_\Omega$ of $\sim 0.1\%$, we shall take $d\Omega < 0.001$, which is roughly f/30 optics.

(*) The pulse width of the mode-locked laser output is about 3 ns (see figure III.6 or Feldman and Figueira , 1974). The line-width is obtained by taking the inverse of the pulse width, which is consistent with the inhomogeneous Doppler broadening at this temperature and pressure.

IV-B-3 Increase of Signal Level

The signal level S is proportional to the scattered photon number :

$$S \propto N_s = \left(\frac{d\sigma}{d\Omega}\right) \times N_e \times L \times N_i \times d\Omega \times F \qquad (IV.3)$$

In this formula, the differential cross section is fixed by the scattering geometry and beam energy; the electron density is determined by the vacuum diode design and the accelerator; the solid angle is limited by the resolution consideration. Only the interaction length L and incident photon number N_i can be manipulated to increase S.

Photon number N_i is maximized by pumping both oscillator and amplifier laser at full voltage (30 KV & 40 KV). The spot size of the laser beam is focused down to match the cross sectional area of the electron beam in the drift tube so that the filling factor F (overlap of optical and electron beam) is close to 1. The scattering length L is chosen to be about 1 cm for reasons to be made clear later in this section.

Taking the electron density $N_e = 3 \times 10^{11}$ cm^{-3} (section V-B), the number of photons scattered into the observation cone is estimated to be

$$N_s / N_i = 3 \times 10^{-15}$$

IV-B-4   Reduction of Noise Level

A series of tests is conducted to look into the possible origins and characteristics of noise. The results are shown in figure IV.1. The signal detected by the photomultiplier working at 2.5 KV with a 100 $\overset{o}{A}$ filter in front is shown in figure IV.1 (d). This signal is a combination of three parts (Figure IV.1): (a) scattered signal (100 mV), (b) visible stray light (10 V), and (c) X-ray induced noise (100 mV).

The dominating part of the noise is the visible background light picked up by the optical system. Several mechanisms are responsible for this high visible noise level: ionization of the background neutral atoms; formation of cathode plasma when whiskers on the cathode tip explode due to Joule heating from the field emission current; sparks made when the incident 9.6μm radiation travels on axis hits the beam dump.

An additional pump line is added to pump the interaction region from both ends to reduce the ionization radiation. The upstream pressure in the drift tube is in the range 10^{-4} to 10^{-5} torr; the electron beam is then at least 95% non-neutral.

The 9.6μm radiation is introduced into the drift tube oriented 1° off-axis so that the incident light not scattered by the electron beam misses the cathode, and hits the beam dump. This oblique incidence method also prevents the cathode plasma, which is formed should the laser beam hit the diode, from shorting out the diode in case the laser pulse arrives too early. The scattered beam line is also tilted 1° off-axis to reduce

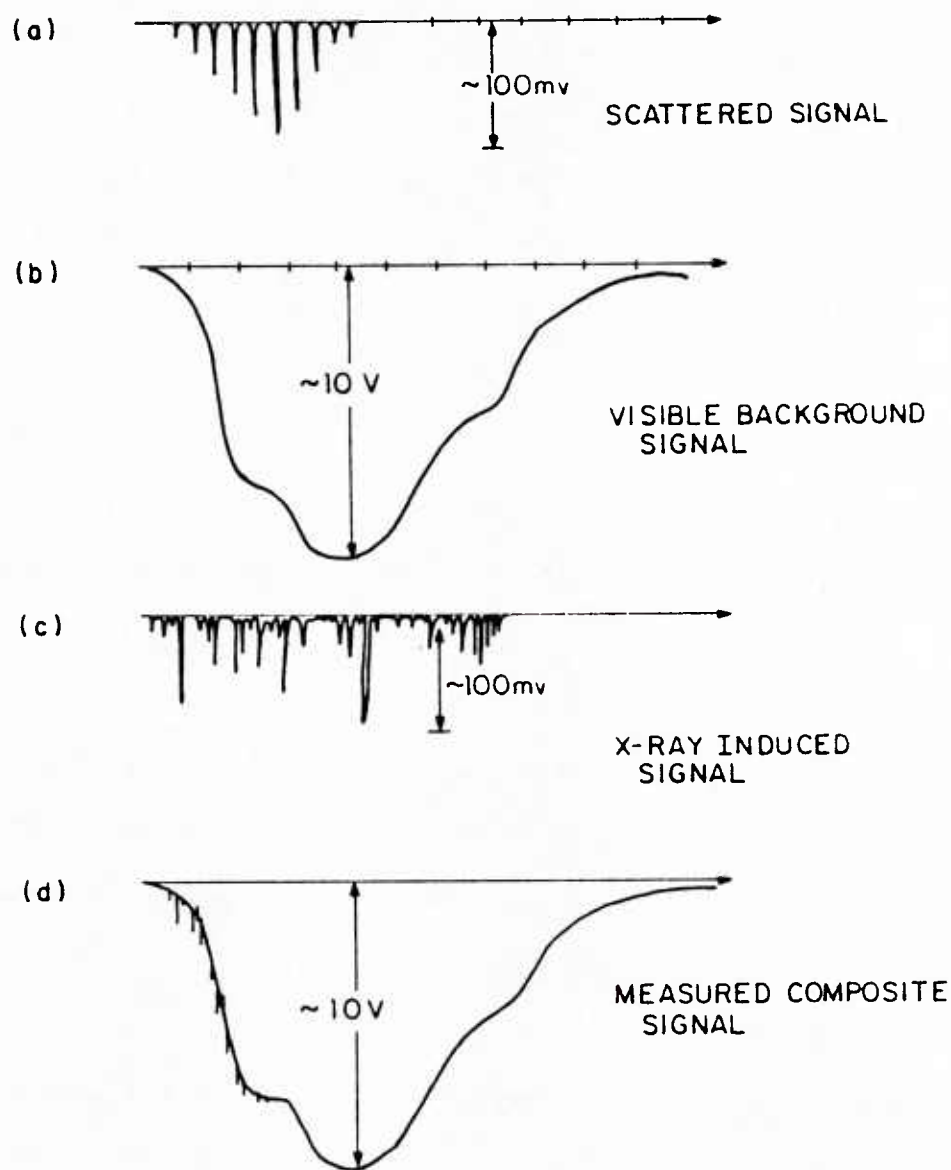Figure IV.1   Waveforms of (a) scattered signal
                         (b) visible background
                         (c) X-ray induced noise
                         (d) combined signal

Figure IV.2
Thermal sensitive
paper diagnostics for
   (a) electron beam spot
   (b) CO_2 laser beam spot

visible light pickup from the diode and the TEA laser beam dump. An aperture stop is used in the output optics to eliminate part of the light not coming from the scattering center (Figure III. 13). This cross-beam arrangement and the slightly converging CO_2 radiation limit the effective scattering length to be about 1 cm. Details of the alignment scheme are described in next section.

After these measures are taken, the 100 mV scattered signal is still easily overwhelmed by the visible stray light. However, by noticing the different temporal characteristics of these two signals (Figure IV.1 (a),(b)), a Hewlett Packard high pass filter 11668A with a 3 dB frequency at 50 MHz is used in the output circuit to filter out the slow-rising stray light noise pulse. This filter works accurately as long as the visible noise pulse is kept well below the saturation level (~ 12 V) of the PMT.

X-rays are generated in the diode region where electrons are accelerated or dumped into the anode, and near the end of the drift tube where the beam is deflected to the wall. In spite of the intensive lead shielding (Section III-E), hard X-rays still penetrate the detector box, strike the Pyrex entrance window and the dynodes of the photomultiplier. This phenomena induces some single photon responses in the detector, and results in a noise signal whose temporal structure is a string of randomly spaced sharp spikes (Figure IV.1 (c)). This spiky noise signal is comparable in magnitude with the genuine scattered signal, and tends to cause difficulties in interpreting the scattering results. Besides the lead shielding around the detector box, another one inch thick lead jacket for the cylindrical photomultiplier was cast to reduce X-ray penetration. The tube

voltage is optimized at 2500 V for higher S/N. The X-ray induced noise is minimized by orienting the detector tube to look at the "quietest" direction in the shielded room. In this experiment, the X-ray noise is cut down to acceptable level (see Fig. IV-4).

Combining these features, the S/N of the system was brought up to more than 5.

IV-C   Alignment and Timing

IV-C-1   Alignment Of The Electron Beam

It is seen in figure III.12 that one end of the drift tube is centered with the anode hole, the other end is supported by two threaded rods. By adjusting these rods, the drift tube is aligned parallel to the guiding field lines. The well centered damage pattern (Figure IV.2(a)) on the witness thermal paper shows the apertured electron beam is guided on the axis of the dift tube.

IV-C-2   Incident Beam Line

An alignment jig made up of a tiny mirror mounted at 45° in a 5mm i.d. tube (Figure III.12) is inserted into the interaction region with the mirror centered on drift tube axis. Light coming from a 24 W bulb above the jig is propagated down and is deflected by the mirror ; it travels along the axis and simulates the scattering center.

When a mask of clear plastic with a cross mark is attached to the NaCl entrance window (Figure III.12), light from the optical jig casts a shadow of the mark outside the drift tube. The trace of the center of the mark shadow defines the incident beam line. A piece of heat-sensitive paper is placed near the center of the interaction region to monitor the laser beam location, and the witnessed thermal pattern will show when the laser beam is right on axis (Figure IV.2(b)). The oblique incidence angle is determined by the position of the cross mark on the mask. The optical jig and the mask are moved out of beam line when running the scattering experiment.

In order to diagnose the large aspect ratio electron beam, an optical system of f/120 is employed. The high power density of the laser requires the first mirror to be placed about 4 meters away from the laser system. These factors result in a 25 meter optical path for the incident beam line. Folding mirrors are used to fit this long focal length system into the relatively small space available. The vibration of the mirrors causes an extra problem when the electron beam machine is fired. A special platform that holds some of the the mirrors was made, which slides in and out of place easilly so that the beam machine can be accessed for cleaning . With this platform in place the vibration problem is minimized, since no mirror is mounted on the same base structure as the accelerator.

IV-C-3   Scattered Beam Line

The incident radiation passes through the upper part of the

NaCl window and hits the lower part of the laser beam dump. The scattered beam line shares the salt window by using the lower part of it (Figure III.12), and looking at the upper portion of the lucite dump.

The light from the optical jig is a perfect simulation of the scattered signal. Because it is visible , this light is relatively easy to manipulate for background reduction and for beam size control (Section III-E).

IV-C-4   System Timing

The four building blocks of this experiment - CO_2 Laser system, Electron beam machine, undulator field, and the detector- have to be fired in proper sequence to produce successful scattering results. The scattering process is initiated manually by generating a main trigger pulse, which then feeds three seperate circuits (Figure IV.3).

One part of this pulse is delayed and amplified to fire a Thyratron switch, which releases the energy stored in the capacitor bank to energize the undulator magnet. The 10 μs rise time of the magnetic field is long compared with the 150 ns electron beam duration, and presents no timing problem to the experiment.

The second part of the main trigger pulse is also amplified and delayed to drive a HV transformer, which triggers the CO_2 TEA laser amplifier. The gain of this laser amplifier remains high for more than 1 μs, so the 120 ns oscillator output pulse is
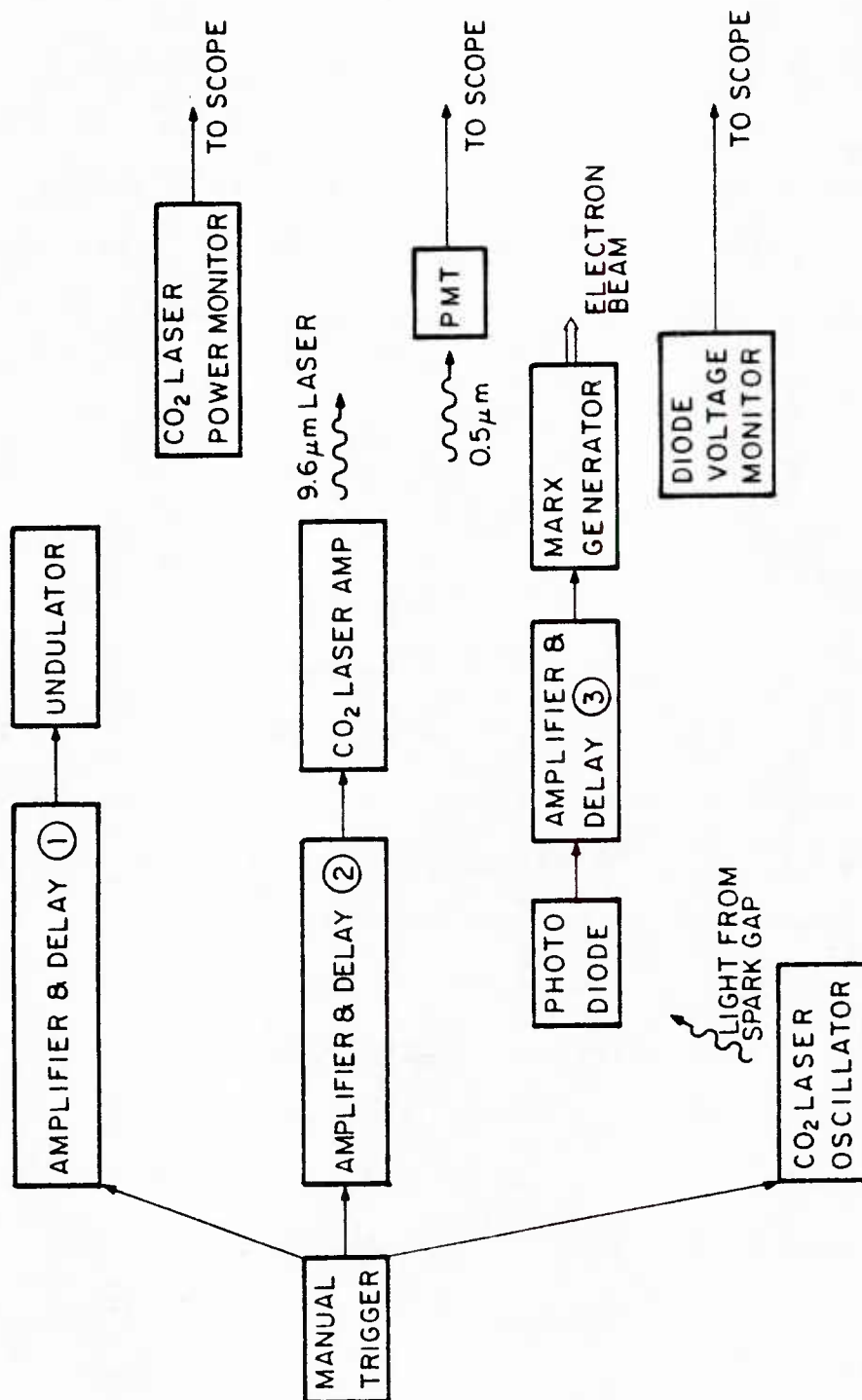
Figure IV.3 System timing sequence

easilly captured and amplified.

The third part of the main trigger signal goes into another high voltage circuit to trigger the oscillator TEA laser spark gap. The time lag between the breakdown of the spark gap and the lasing of oscillator is very sensitive to the pressure in the spark gap, the gas combination in the laser cavity, and the pumping voltage. For a particular set of operating parameters (*), this time lag is relatively constant: the light emitted by the spark gap can be treated as the forerunner of the laser output.

This spark gap light is picked up by a photo diode detector, then boosted in voltage to drive a delay generator. This delayed signal then triggers the Marx generator and the electron beam. The scattered signal, the CO2 laser power signal, and the diode voltage signal, are sent to oscilloscopes in the shielded room. All scopes are triggered by the diode voltage signal.

In figure IV.3, it is seen that delay-1 is responsible for laser-undulator timing; delay-2 matches the relative firing time of the two lasers; delay-3 takes care of the electron beam-laser beam synchronism.

(*) Oscillator: operating at 30 KV, He:N :CO_2 = 25: 2: 6, spark gap pressure: 15 pounds of CO_2 .
Amplifier : operating at 40 KV, He:N :CO_2 = 8: 1: 3, spark gap pressure: 30 pounds of dry air.

The short-pulse character of the laser and the electron beam requires a time jitter as low as 50 ns. It is not easy to operate the system with such a low jitter since a large number of gas switches and spark gaps are used in both laser system and electron accelerator (Sections III-B,C).

An example of a successful shot is shown in figure IV.4. The upper trace in both pictures shows the diode voltage. The photon drag signal is delayed to compensate for the shorter signal propagation time so that the laser beam actually intercepts the electron beam when it appears so on the scope. The scattered signal is delayed an extra 35 ns by the transit time effect of the photomultiplier. The high pass filter differentiates the PMT output, yielding a signal with both positive and negative parts.

IV-D   Interpretation of Scattering Results

When a finite bandwidth signal I(w) passes through a filter with response function T(w), the transmitted signal is

$$S = \int I(w) \, * \, T(w) \, dw \qquad (IV.4)$$

From the dicussion in II-C, the scattered spectrum for a relative cold beam will be approximated by a narrow Gaussian with a width Δw

$$I(w) = I \, * \, e^{-\left(\frac{\omega-\omega_s}{\Delta\omega}\right)^2} \qquad (IV.5)$$
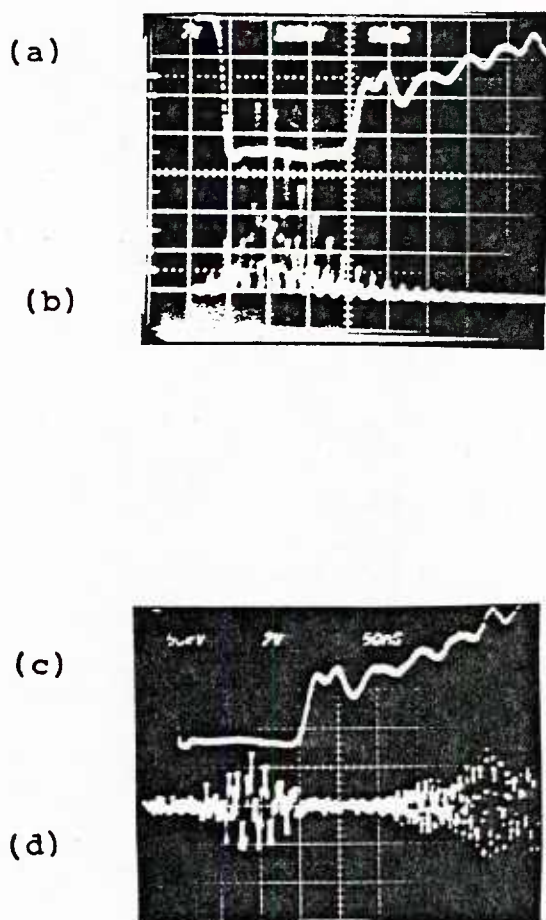
Figure IV.4 (a) diode voltage, 200 KV/div, 50 ns/div
            (b) CO_2 laser power monitor, 5 MW/div, 50 ns/div
            (c) scattered signal, 50 mV/div, 50 ns/div

If the filter transmission is "ideal", then T(w) can be written

as $\quad T(w) = T * e^{-\left(\frac{\omega - \omega_s}{\Delta f}\right)^2}$ (IV.6)

Then $\quad S(w, f) = I\, T \int_0^\infty e^{-(\omega - \omega_s)^2 \left[\frac{1}{(\Delta f)^2} + \frac{1}{(\Delta \omega)^2}\right]} d\omega$ (IV.7)

$$= I\, T \sqrt{\pi} \sqrt{\frac{(\Delta \omega \cdot \Delta f)^2}{(\Delta \omega)^2 + (\Delta f)^2}}$$ (IV.8)

Throughout the following analysis, bndwidths at full width half maximum (FWHM) are used in all spectral and filter widths, so an extra factor of $\sqrt{2\ln 2}$ will be needed hereafter.

Since beam energy spread is related to spectral width by

$\left(\frac{\Delta \gamma}{\gamma}\right)_{\parallel, inhomo} = \frac{\beta}{2}\left(\frac{\Delta \omega}{\omega}\right)_{inhomo}$, equation IV.8 can be rewritten in terms of

$$S\left(\left(\frac{\Delta \gamma}{\gamma}\right)_{\parallel}, \Delta f\right) = \frac{b \cdot \left(\frac{\Delta \gamma}{\gamma}\right)_{\parallel} \cdot \Delta f}{\sqrt{a^2 \cdot \left(\frac{\delta \gamma}{\gamma}\right)_{\parallel}^2 + (\Delta f)^2}}$$ (IV.9)

, where $a = \frac{2\omega_s}{\beta}$, $b = I \cdot T \sqrt{2\pi \ln 2} \cdot a$

This function is plotted in figure IV.5, which shows the dependence of the transmitted signal levels on $\left(\frac{\delta \gamma}{\gamma}\right)_{\parallel}$ and filter bandwidth Δf.

However, the filters used in the experiment were not "ideal". A grating spectrometer was set up to determine the transmission characteristics of these interference filters. Figure IV.6 shows the results. In a more general sense, the PMT spectral response is also incorporated into these curves. However
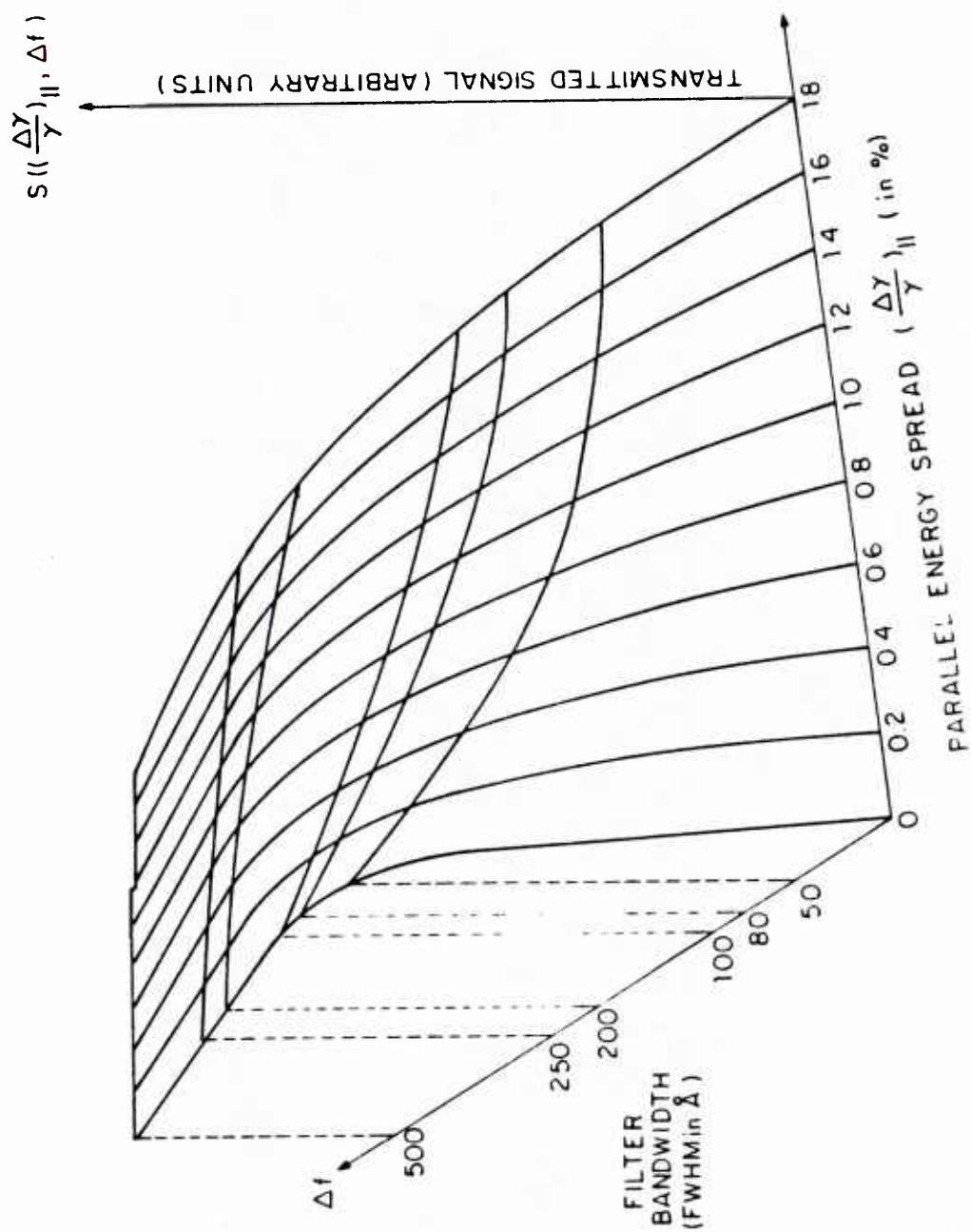
Figure IV.5 Transmitted signal level versus filter bandwidth for various beam energy spreads (Gaussian filters)
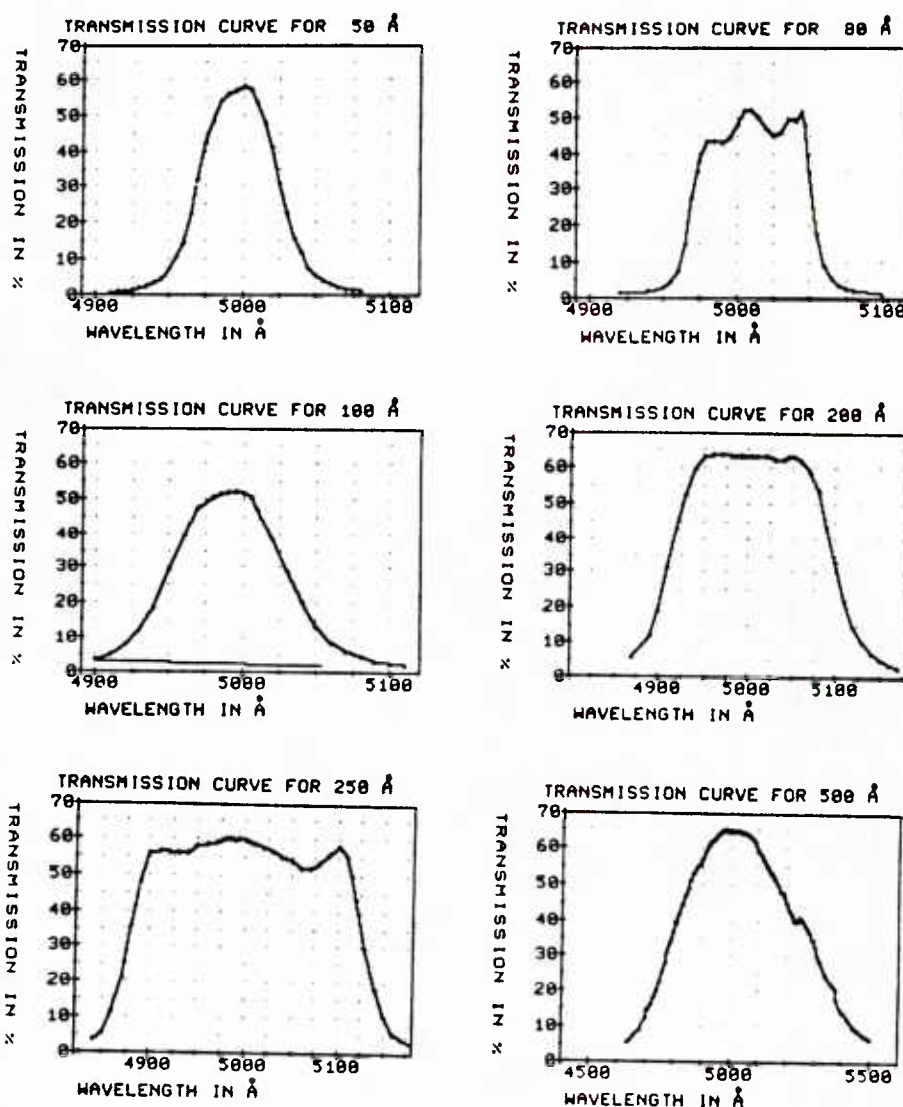
Figure IV.6   Transmission characteristics for filters used in experiment

the   response is relatively flat in this narrow spectral   region. The integration in equation IV.4 is carried out numerically using these actual T(w)'s. In this case, each $\left(\delta\gamma/\gamma\right)_{\parallel}$ has only six filter points. A graph (Figure IV. 7) is generated as the real-filter counterpart of figure IV.5. The line between points is connected for easy identification of these points.

Data are accumulated by cataloging "good" shots[*] taken under the same alignment condition and diode voltage with various filters in front of the detector. These signals are first normalized to the corresponding incident laser power level, whose shot-to-shot variation is about 30%, then the correlation between these data points is carefully compared with those of the point-sets in figure IV.7. The curve that fits the scattered data best then yields the experimentally measured $\left(\delta\gamma/\gamma\right)_{\parallel}$.

Once the $\left(\delta\gamma/\gamma\right)_{\parallel}$ is determined, each data point is multiplied by a correction factor -the ratio of ideal transmitted signal to realistic one-,   that is, data are renormalized with respect to the corresponding ideal-filter curve. Thus scattering results are presented graphically, such as figure V.1, which shows the smooth "expected" function S(Δf) and the six experimental points for this particular $\left(\delta\gamma/\gamma\right)_{\parallel}$.

[*]

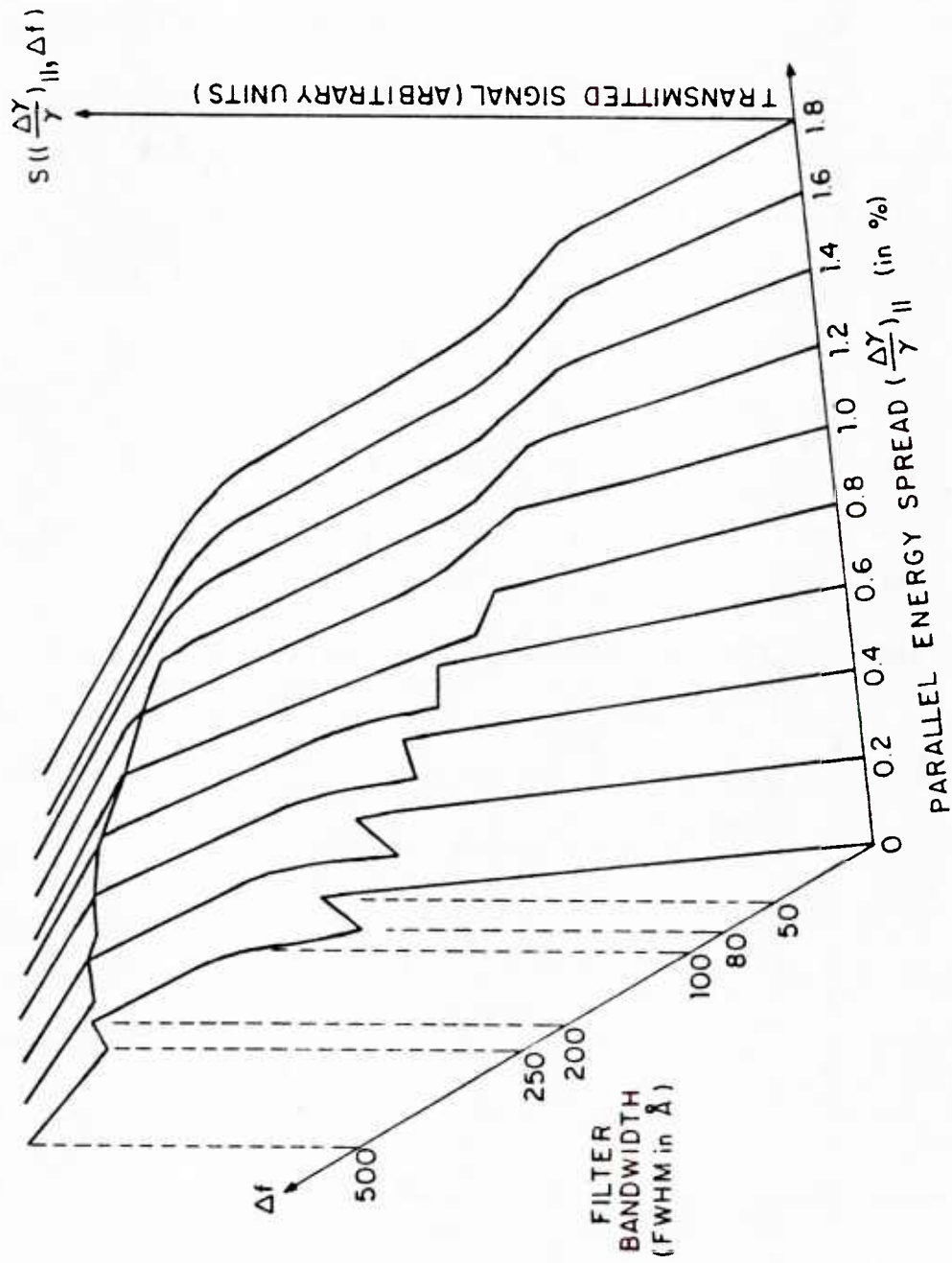About 80 of the 250 shots were "good" shots, in which 120 "spikes" were used to determine the spectral widths.

Figure IV.7 Transmitted signal level versus filter bandwidth for various beam energy spreads (real filters)

Chapter V

EXPERIMENTAL RESULTS

V-A   Introduction

The inhomogeneous broadening caused by the space charge effect and the inherent beam emittance is measured on the electron beam described in section III-C, propagated down the drift tube, guided by a 9.5 KG field, without any wiggler exitation.

The scattered spectral width is determined by deconvoluting the filter (and the photomultiplier) response from the measured signal using the correlating procedure described in section IV-D. Four values of undulator field strength were used to study the additional parallel energy broadening caused by the radial gradient of the undulator field, the results showed (within error limit) that the undulator inhomogeneous broadening combines with other inhomogeneous broadening mechanisms as the RMS sum.

The measured total parallel momentum spread in all cases is smaller than the limitation imposed by the collective interaction criterion (see section I-B), and the beam is accordingly found suitable for the Raman FEL application.

V-B   Scattering Results

V-B-1   Zero Undulator field

In chapter I we have shown that without undulator exitation, the major causes of the beam parallel energy spread come from the inherent transverse motion (the diode emittance) and the space charge potential across the beam radius. The emittance contribution for zero undulator field is

$$\left(\frac{\delta\gamma}{\gamma}\right)_{\parallel,\varepsilon} = \frac{1}{2}\left(\frac{\varepsilon_N}{r_b}\right)^2 \tag{V.1}$$

, while the space charge depression causes a spread of

$$\left(\frac{\delta\gamma}{\gamma}\right)_{\parallel,\,s.c.} = \frac{\omega_{po}^2\, r_b^2}{4\gamma c^2} \tag{V.2}$$

, where r_b is the radius , and ω_{po} is the plasma frequency of the electron beam (*).

The result obtained for five different filters shows a total parallel energy spread of 0.6 % $\pm$ 0.14 % (Figure V.1). In the figure the five normalized data points are shown together with the dotted "0.6 % spread" curve chosen from figure IV.5. Each filter point is an average of several shots taken under nearly identical conditions of accelerator performance. A larger error bar is associated with the 500 $\overset{\circ}{A}$ point because the increased filter bandwidth let in more background light while the

---

(*) The beam electron density is determined by a Faraday cup current measurement or by the argument given in the end of this section.
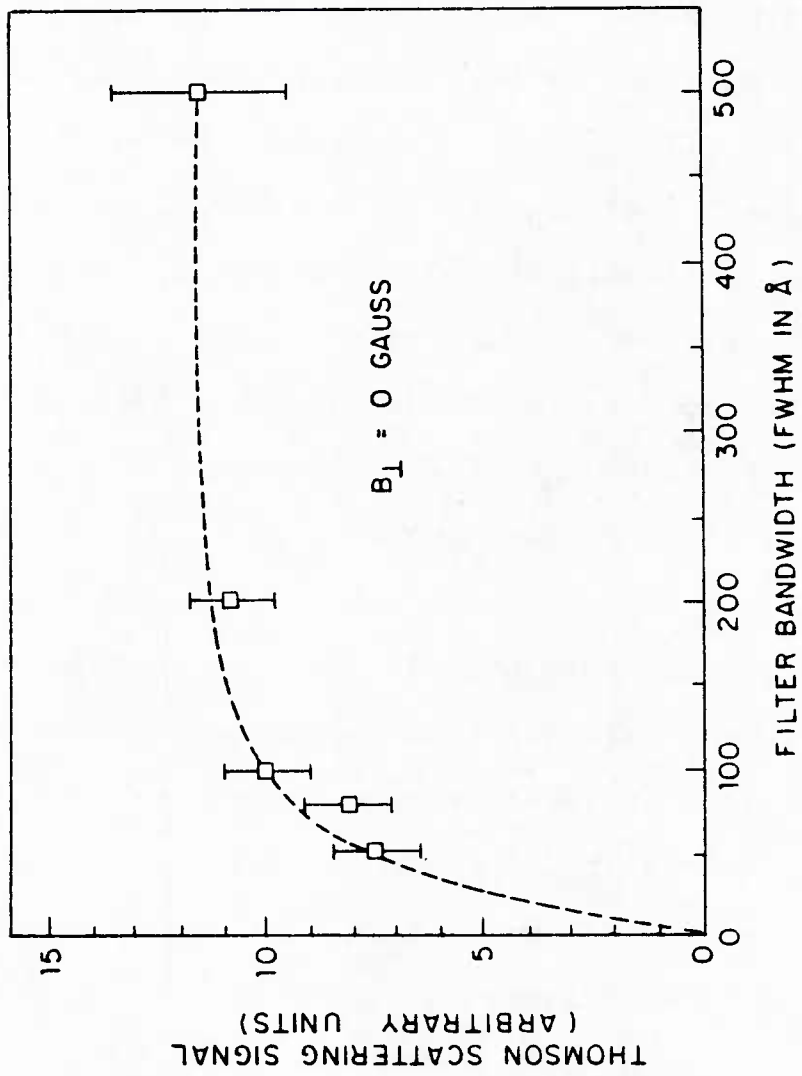
Figure V.1 Scattered results for 0 Gauss undulator field

scattered signal remains at the same level (note the leveling-off feature at large filter bandwidth in figure IV.5). The fact that changing the diode voltage by ~ 2 % (at filter Δf = 100 Å) causes the scattered spikes to disappear provides supporting evidence that we are dealing with a narrow bandwidth signal.

The difference between the measured total spread 0.6 % and the estimated space charge contribution 0.5 % provides a rough estimation for the emittance contribution. A diode emittance of 0.3 % is estimated if the emittance and the space charge broadening mechanisms are assumed to act on the electrons independently (Equation I.14); the 0.6 % spread is equivalent to a total normalized emittance of $\mathcal{E}_N$ = 20 π·mrad.cm. This is to be compared with the NRL computational analysis (R. Jackson et al., 1983) for a similar diode design (which ours was adopted from) in which they predicted a $\mathcal{E}_N$ = 30π·mrad.cm under a somewhat different accelerator and guiding condition.

Knowledge of the electron beam density can be inferred from the experimental parameters as follows: the frequency upshift factor 19.2 signifies an average beam energy of 670 KV is involved in the scattering, while a well-calibrated (*) measurement (see section III-C) of accelerating diode voltage gave 700 KV. The 30 KV difference is apparently due to the space charge potential depression of the beam. The beam electron

----

(*) The accuracy of the diode voltage measurement is determined by the resolution of the electrostatic voltmeter and the oscilloscope, which is 0.2 % and 0.5 % ,respectively.

density is then estimated to be 3×10^{11} cm^{-3}.

It is interesting to compare the observed signal level with that predicted by equation (II.12). The comparison involves some quantities that are not measured directly: the electron density, the effective scattering length, the filling factor of the two beam profiles, the optical losses, the quantum efficiency and current gain of the photomultilier, etc. However, a zeroth order estimation shows that the scattered power is of the expected order (See figure V.2 for a table of the estimated experimental parameters): the ratio of number of scattered photons per unit time to the number of incident photon per unit time into the solid angle $d\Omega$ is

$$(\dot{N}_s / \dot{N}_i) = (\frac{d\sigma}{d\Omega}) \times d\Omega \times n_e \times \ell \times a \qquad (V.3)$$

where $\dot{N}_i = P_i / \hbar w_i$. The expected signal voltage into a 50Ω scope is

$$S = \dot{N}_s \times \alpha \times \eta \times e \times g \times \beta \times 50 \qquad (V.4)$$
$$\sim 0.3 \text{ (volts)}$$

this is to be compared with the experimentally observed 0.1 volt.

V-B-2   Finite Undulator Field

The axial quiver motion induced by the FEL interaction is a second order quantity (Freund et al., 1981) and is negligible in the experiment. The main effect of the undulator on the beam is

$\dfrac{d\sigma}{d\Omega}$	differential cross section	$1.5 \times 10^{-24} cm^2$
$d\Omega$	observation solid angle	$\sim 5 \times 10^{-4}$
n_e	electron density	$\sim 3 \times 10^{11} cm^{-3}$
ℓ	effective scattering length	~ 1 cm
a	alignment factor	~ 0.5
P_i	incident laser peak power	~ 20 MW
$\hbar\omega_i$	9.6 μm photon energy	0.13 eV
α	optical loss factor	~ 0.3
η	PMT quantum efficiency	~ 0.2
g	PMT current gain	$\sim 10^7$
β	high pass filter attenuation	~ 0.5

Figure V.2   Table of experimental parameters used to estimate
scattered signal level

the nonuniform pumping process described in section I-D, which heats up the beam in both transverse and longitudinal direction.

The anticipated undulator contribution to the momentum spread is

$$\left(\frac{\delta \gamma}{\gamma}\right)_{\|,und} \cong (\gamma \beta_\perp)^2 \cdot \left(\frac{\Delta B_\perp}{B_\perp}\right) \qquad (V.5)$$

where $\Delta B_\perp / B_\perp$ represents the variation of field amplitude across the beam radius. The field variation is about 20 % for the 17 mm period undulator across the 2.5 mm radius beam used in the experiment. The transverse velocity for particles pumped by a circularly polarized undulator field and at the same time gyrating in a logitudinal guiding field is given by

$$\beta_\perp = \frac{e B_\perp \ell}{2\pi m c^2 \gamma} \cdot \left| \frac{e B_0 \ell}{2\pi m c^2 \gamma} - 1 \right|^{-1} \qquad (V.6)$$

where the term in the absolute value brackets is the enhencement of motion from operating the system near the undulator-guide field "magnetoresonance"

$$\frac{2\pi \gamma v_\|}{\ell} = \frac{e B_0}{m c} \qquad ; \qquad (V.7)$$

for a guiding field of 9.5 KG, this enhancement factor is about 4. Therefore, besides the emittance and space charge part, an additional undulator-caused momentum spread of 0.3 %, 0.8 %, 1.9 % is expected respectively for $B_\perp$ = 225 G, 375 G, 525 G. A table summarizing the undulator field, the computed transverse velocity , various expected beam momentum spreads and the measured total spread is given in figure V.3. The emittance term is not included

because it is not obtained from first principles and is not measured independently (see section V-B-1).

The Thomson scattering results for different undulator fields are shown in figures V.4 to V.6. As the beam gets hotter, the scattered power will spread out the spectrum to such an extent that filters with narrow bandwidth cannot transmit enough signal to be clearly detected (note the absence of 50 $\overset{o}{A}$ data in figure V.6), given the system noise level.

The expected dependence of beam energy spread on the undulator-induced transverse velocity alone (Equation V.5) , and the dependence with the space charge and emittance contribution incorporated are shown in figure V.7. The total energy spread measured in the experiment is shown to be in good agreement with the estimated curve, obtained by combining the space-charge and undulator terms as the RMS sum ,(viz, as random effects).

One interesting point should be noted here: the electron beam space charge term causes electrons inside the beam to have less forward energy than electrons on the outside; whereas, the undulator pumps more efficiently on the outside of the beam in converting parallel velocity to transverse motion. These two effects seem to be in opposite tendency, which means there exists an optimum undulator field which induces maximum cancellation of broadening effects and results in a monoenergetic beam. However,

$B_\perp$ (G)	$V_\perp/C$ QUIVER	MEASURED $(\frac{\delta\gamma}{\gamma})_\parallel$ (TOTAL)	ESTIMATED		
			$(\frac{\delta\gamma}{\gamma})_\parallel$ S.C.	$(\frac{\delta\gamma}{\gamma})_\parallel$ und.	$[(\frac{\delta\gamma}{\gamma})^2_\parallel \text{s.c.} + (\frac{\delta\gamma}{\gamma})_\parallel \text{und}]^{\frac{1}{2}}$
000	0.0	0.6% ± 0.14%	0.5%	0.0%	0.5%
225	0.055	0.8% ± 0.14%	0.5%	0.3%	0.77%
375	0.10	1.1% ± 0.14%	0.5%	0.8%	0.9%
525	0.15	1.9% ± 0.14%	0.5%	1.9%	2.06%

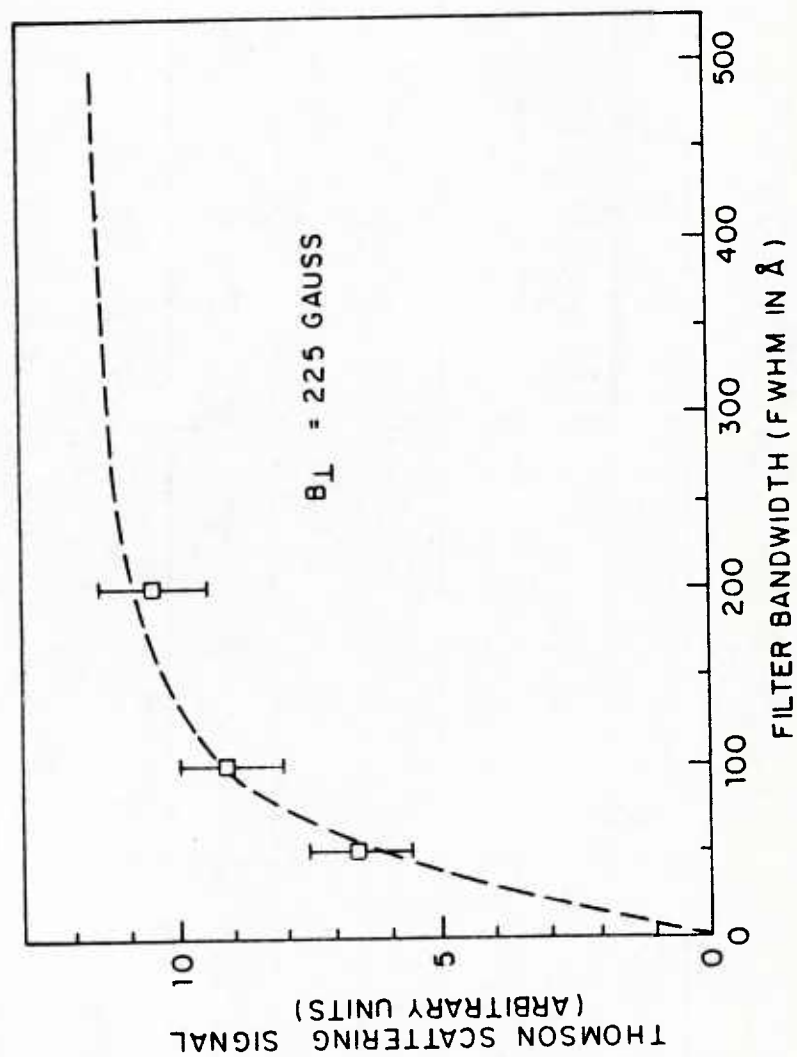Figure V.3 Table of various beam energy spreads

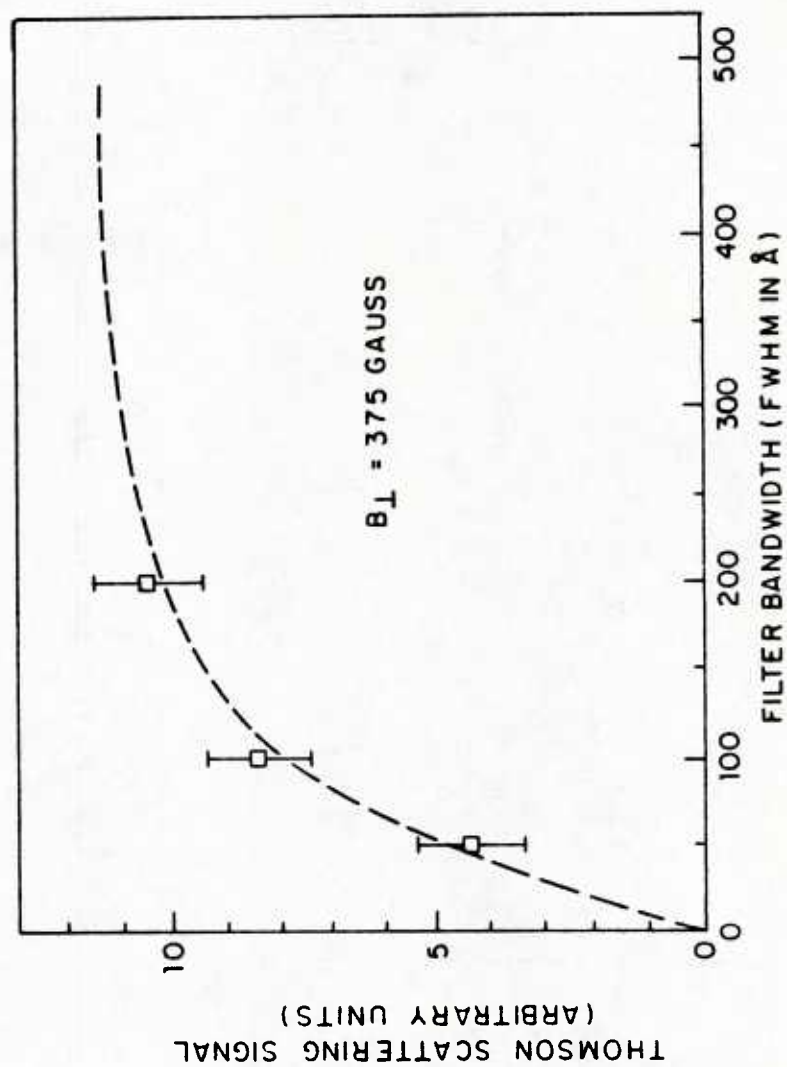Figure V.4   Scattered results for 225 Gauss undulator field

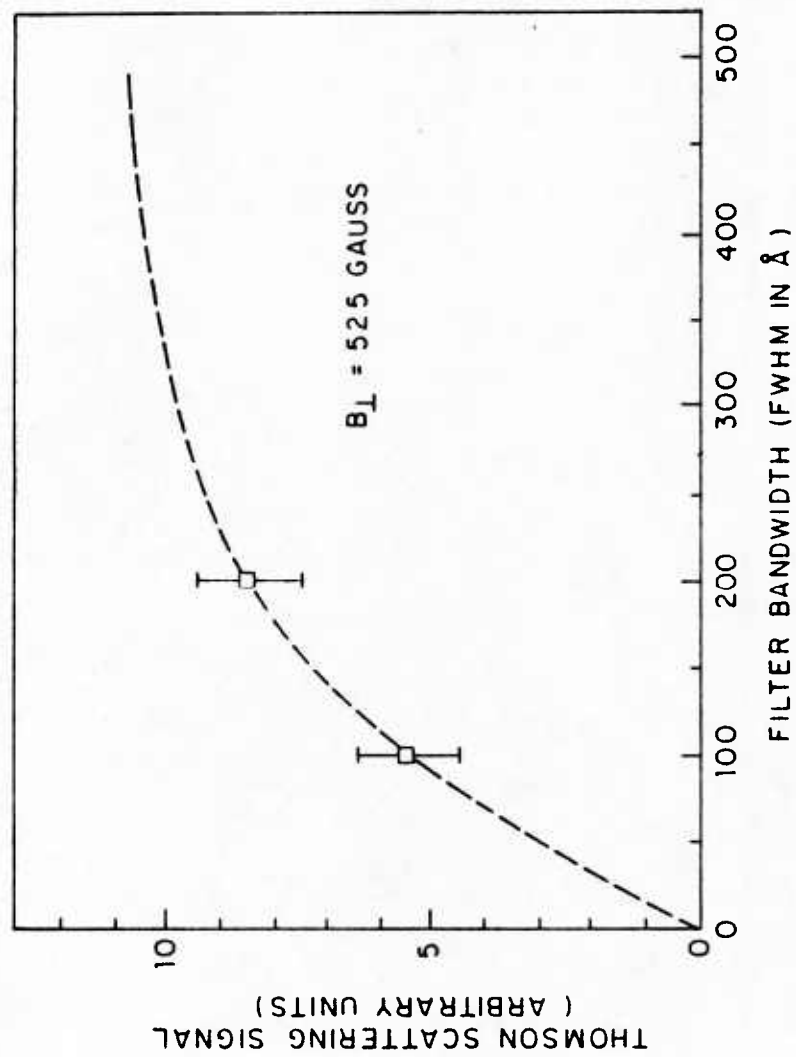Figure V.5   Scattered results for 375 Gauss undulator field

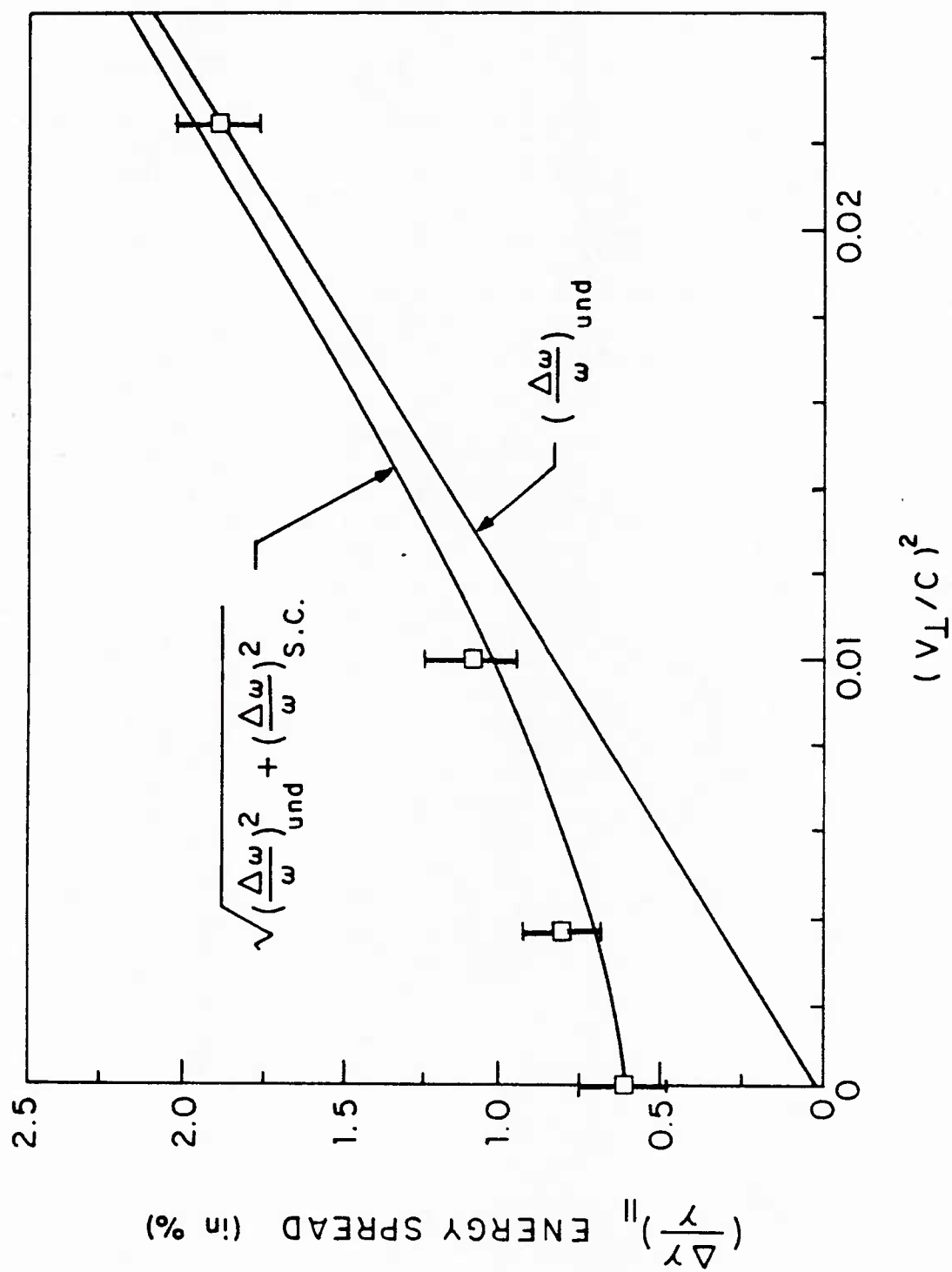Figure V.6   Scattered results for 525 Gauss undulator field

Figure V.7 Dependence of beam parallel energy spreads on the transverse velocity

this cancellation effect has never been observed in our experiment(*).

The result of the single channel data shows a parallel energy spread as small as 0.6 % is obtained for the electron beam generated by the specially designed diode. The spread increases monotonically as the undulator coil is energized, but the spread remains < 2 % for a beam with a $\beta_\perp$ < 0.15.

(*) Linear combination (with different signs) of the estimated broadenings was also compared with experimental data. Only the RMS sum fits the monotonically increasing energy spread well.

Chapter VI

CONCLUSION

An non-interactive Thomson backscttering experiment was designed and used to diagnose an intense relativistic electron beam (IREB) in a Raman free electron laser. The single channel spectral system is capable of resolving a $\Delta\omega/\omega$ of 0.1 %. The parallel energy spread of the 700 KV, 1 KA/cm^2 magnetized beam was determined to be 0.6 %.

When used with an undulator, the beam heats up monotonically with increasing undulator field amplitude. The beam is suitable for Raman free electron laser application since the energy spread remains smaller than the collective interaction criterion (2 % in our case, i.e. $\sim$ 1/2N) even when the beam is pumped to the trnsverse velocities > 0.1 C , which should result in high gain (*). The operation of a high gain, high efficiency collective FEL in the submillimeter spectral region is highly feasible, as indeed recent experimentation has demonstrated.

The theory of Thomson scattering was reviewed with two approaches: (1) quantum electrodynamic calculation of Compton

----

(*) The experimental results (figure V.7) show that the parallel energy spread remains less than 2 % for $\beta_\perp$ < 0.15 C. The maximum spatial growth rate for such a low-spread beam is predicted to be about 0.14 cm^{-1} by a theoretical analysis (Ibanez, 1983). A single pass gain as high as 30 dB should be obtained for a 50 cm long undulator operating under ideal conditions.

scattering in the long wavelength limit , and (2) a classical treatment of plane waves scattered by relativistic electrons. The polarization effects as well as other corrections (retarded time , flux compression) were treated properly and these two forms of scattering cross section were shown to be mutually consistent.

Besides the non-interactive feature commom to all Thomson scattering experiments, there are some attractive merits unique to this experiment, which benefit from the relativistic effects and the backscattering geometry:

(1) The scattering cross section is enhanced relativisticly by a factor of $4\gamma^2$ (Section II-B-2). Since the electron density in IREBs is small compared to that of the plasma diagnostic experiments, the enhancement is helpful in obtaining a reasonable signal level.

(2) A maximum frequency upshift of $4\gamma^2$ is provided by the back scattering geometry, which eliminates the problem of detecting an overlapped incident and scattered spectrum . This is true for a plasma (or an IREB) moving with high average velocity.

(3) Comparing the scattering of radiation from particles with zero and with a high average velocity into same wavelength region, the incident photon number provided by lasers of same power level, is more plentiful by a factor of $4\gamma^2$ for the latter case.

(4) A first order extension of the observation solid angle only

introduces a second order broadening effect. The backscatter-
ing geometry offers the best resolution (Section II-B-2).

(5) For any particular velocity spread, the associated scattered
width is maximized-- which means the highest sensitivity is
achieved--using the backscattering geometry. This feature is
essential for detecting a small energy spread (Section II-B-
2).

Historically, Thomson scattering from an electron beam was
first observed for a 2 KV, 75 ma beam (Fiocco and Thompson,
1962). The experiment did not take advantage of the
backscattering geometry and was unable to benefit from the
relativistic effects.

On the other hand, the relativistic effect was used
dramatically in a high energy physics experiment (Sinclair et
al., 1969). The 20 Gev electron beam in SLAC was used as a
frequency up-converter also preserving the polarization of an
incident ruby laser signal to produce polarized 7 Gev photons.

This dissertation records the first use of Thomson
scattering as a diagnostic for the velocity spread of an intense
relativistic electron beam. The measurement indicates the beam
used was cold enough for the collective FEL interaction. With a
properly tapered undulator and an operation domain around the
wiggler-guide gyroresonance, the device is supposed to work with
very high gain and efficiency. Raman free electron laser
amplifier experiment utilizing this cold electron beam to amplify
external FIR laser radiation is now being tested in the Columbia
plasma physics laboratory .

BIBLIOGRAPHY

Akhiezer, A.I., and Berestetskii, V.B. Quantum Electrodynamics
John Wiley & Sons, New York (1965)

Avivi, P., and Cohen, Ch., and Friedland, L "Drift Velocity
Measurements in Relativistic Electron Beams." Applied Physics
Letters 42 (1983): 948

Bjorken, J.D., and Drell, S.D. Relativistic Quantum Mechanics
McGraw-Hill, New York, (1964)

Blewett, J.P., and Chasman, R.C. "Orbits and Fields in the Helical
Wiggler." Journal Of Applied Physics 48 (1977): 2692

Bosco, P., and Colson, W.B. "Spontaneous Radiation from
Relativistic Electrons in a Tapered Undulator." Physical
Review A28 (1983):319

Chen, S.C., Marshall, T.C., and Schlesinger, S.P. "Thomson-
Scattering Experiment to Determine Beam-Parallel Velocity
Spread." Proceedings of the LASERS 1982 Conference (to be
Published)

Chen, S.C., Marshall, T.C., and Schlesinger, S.P. in Proceedings
of the 1983 Free Electron Laser Workshop (unpublished)

Chen, S.C., Marshall, T.C., and Schlesinger, S.P. "Determination
of Parallel Velocity Spread of an Intense Relativistic
Electron Beam by Thomson Scattering." Bulletin of the
American Physical Society 28 (1983): 1062

Chen, S.C., and Marshall, T.C. "Thomson Backscattering from a
Relativistic Electron Beam as a Diagnostic For Parallel
Velocity Spread." Physical Review Letters 52 (1984): 425

Colson, W.B. "One-Body Analysis of Free Electron Lasers." Physics
of Quantum Electronics 5 (1977): 157

Colson, W.B.; and Ride, S.K. "The Free-Electron Laser: Maxwell's
Equations Driven by Single-Particle Current." Physics of
Quantum Electronics 7 (1980): 377

Colson, W.B. "Optical Pulse Evolution in the Stanford Free-
Electron Laser and in a Tapered Wiggler." Physics of Quantum
Electronics 8 (1982): 457

Davis, H., and Willi, O. "Laser Scattering from an Intense
Relativistic Electron Beam." Bulletin of the American
Physical Society 28 (1983): 1040

Deacon, D.A.G.; Elias, L.R.; Madey, J.M.J.; Ramian, G.J.; Schwettman, A.; and Smith, T.I. "First Operation of a Free Electron Laser." Physical Review Letters 38 (1977): 892

Efthimion, P.E., and Schlesinger, S.P. "Raman Scattering by an Intense Relativistic Electron Beam in a Long Rippled Magnetic Field." Physical Review 16A/2 (1977): 633

Elias, L.R.; Fairbank, W.M.; Madey, J.M.J.; Schwettman, H.A.; Smith, T.I. "Observation of Stimulated Emission of Radiation by Relativistic Electrons in a Spatially Periodic Transverse Magnetic Field." Physical Review Letters 36 (1976): 717

Feldman, B.J., and Figueira, J.F. "Generation of Subnanosecond CO_2 Laser Pulses at 10.6 um by Pulse Compression Techniques." Applied Physics Letters 25 (1974): 301

Fiocco, G., and Thompson, E. "Thomson Scattering of Optical Radiation from an Electron Beam." Physical Review Letters 10 (1963): 89

Freund, H.P.; Sprangle, P.; Dillenburg, D; daJornada, E.H.; Liberman, B.; and Schneider, R.S. "Coherent and Incoherent Radiation from Free Electron Lasers." Physical Review A24 (1981): 1965

Friedman, M. Hammer, D.A.; Manheimer, W.M.; and Sprangle, P. Physical Review Letters 31 (1973): 752

Gilgenbach, R.M.; Marshall, T.C.; and Schlesinger, S.P. "Spectral Properties of Stimulated Raman Radiation fron an Intense Relativistic Electron Beam." Physics of Fluids 22 (1979): 971

Hopf, F.A.; Meystre, P.; Moore, G.T.; and Scully, M.O. "Nonlinear Theory of Free-Electron Devices." Physics of Quantum Electronics 5 (1977): 41

Ibanez, L.F., and Johnston, S. "Finite-Temperature Effects in Free-Electron Lasers." IEEE Journal of Quantum Electronics QE-19 (1983): 339

Jackson, R.H., Gold, S.H., Parker, R.K., Freund, H.P., Efthimion, P.C., Granastein, V.L., Herodon, M., Kinkead, A.K., Kosakowski, J.E., and Kwan, T. "Design and Operation of a Collective Millimeter-Wave Free-Electron Laser." IEEE Journal of Quantum Electronics QE19 (1983): 346

Kakushkin, A.B. "Incoherent Scattering of Light by a Finite Volume of a Relativistic Plasma." Soviet Journal of Plasma Physics 7 (1981 a): 63

Kakushkin, A.B. "Polarization Effects in Incoherent Scattering of Light by Relativistic Electrons." Soviet Journal of Plasma Physics 7 (1981 b): 669

Kroll, N.M. "The Free-Electron Laser as a Travelling Wave Amplifier." Physics of Quantum Electronics 5 (1977): 115

Kawai, M., Kawamura, Y., and Toyoda, K. "Discrete Energy Spectrum of an Intense Relativistic Electron Beam." Physics Letters 99A (1983): 387

Kwan, T., and Snell, C.M. "Efficiency of Free Electron Lasers with a Scattered Electron Beam." Physics of Fluids 26 (1983): 835

Landau, L.D., and Lifshitz, E.M. The Classical Theory of Fields , Addison Wesley, Reading, Mass. (1975)

Marshall, T.C.; Talmadge, S.; and Efthimion P.E. "High Power Millimeter Radiation from an Intense Relativistic Electron Beam Device." Applied Physics Letters 31(1977): 320

Madey, J.M.J. "Stimulated Emission of Bremsstrahlung in a Periodic Magnetic Field." Journal of Applied Physics 42 (1971): 1906

Madey, J.M.J. "Relationship between Mean Radiation Energy, Mean Squared Radiated Energy and Spontaneous Power Spectrum in a Power Series Expansion of the Equation of Motion in a Free-Electron Laser." Nuovo Cimento 50B (1979): 64

McDermott, D.B.; Marshall, T.C.; Schlesinger, S.P.; Parker, R.K.; and Granatstein, V.L. "High Power Free Electron Laser Based on Stimulated Raman Backscattering." Physical Review Letters 41 (1978): 1368

Motz, H. "Application of the Radiation from Fast Electron Beams." Journal of Applied Physics 13B (1951):527

Motz, H.; Thon, W.; and Whitehurst, R.N. in Journal of Applied Physics 24 (1953): 826

Motz, H.; and Nakamura, M. in Annals of Physics 7 (1959): 84

Nee, S.F., and Pechacek R.E., and Trivelpiece, A.W. "Electromagnetic Wave Scattering from a Magnetically Confined High-Temperature Plasma." Physics of Fluids 12 (1969): 2651

Neil, V.K. Jason Report JSR-79-10, (1979) SRI International

Pantell, R.H.; Soncini, G.; and Puthoff, H.E. in IEEE Journal of Quantum Electronics 4 (1968): 905

Pechacek, R.E., and Trivelpiece, A.W. "Electromagnetic Wave Scattering from a High-Temperature Plasma." Physics of Fluids 10 (1967): 1688

Phillips, R.M. "The Ubitron: A High-power Traveling-Wave Tube Based on a Periodic Beam Interaction in Unloaded Waveguides." IEEE Transactions on Electronic Devices 7 (1960): 231

Shefer, R.E., Yin, Y.Z., and Bekefi, G. "Velocity Diagnostics of Mildly Relativistic, High Current Electron Beams." Journal of Applied Physics 54 (1983): 6154

Sheffield, J Plasma Physics 14 (1972): 783

Sheffield, J Plasma Scattering of Electromagnetic Radiation, Academic, New York (1975)

Sheffield, R.L.; Montgomery, M.D.; Parker, J.V. Riepe, K.B.; and Singer, S. Journal of Applied Physics 53 (1982): 5403

Sinclair, C.K., Murray, J.J., Klein, P.R., and Rabin, M. " A Polarized Photon Beam for the SLAC 82-Inch Hydrogen Bubble Chamber." IEEE Transactions on Nuclear Sciences 116 (1969): 1065

Schneider, J. in Physical Review Letters 2 (1959): 504

Ward, G., and Pechacek, R.E., and Trivelpiece, A.W. "Scattering of a Laser Beam by High-Temperature Plasmas." Physical Review A3 (1971): 1721

Ward, G., and Pechacek, R.E. "Scattering of Light by Relativistic Electrons." Physics of Fluids 15 (1972): 2202

Williamson, J.H., and Clarke, M.E. "Construction of Electron Distribution Functions from Laser Scattering Spectra." Journal of Plasma Physics 6 (1971): 211

Zhuravlev, V.A., and Petrov, G.D. "Scattering of Radiation by Finite Volumes of Relativistic Plasma." Soviet Journal of Plasma Physics 5 (1979): 3

Zhuravlev, V.A., and Petrov, G.D. "Scattering of Light by the Electrons of a High Temperature Plasma." Opt. Specktrosk. 33 (1972): 36